








Formation of short-range magnetic order and avoided ferromagnetic quantum criticality in pressurized LaCrGe₃

Elena Gati ^{1,2,*} John M. Wilde ^{1,2} Rustem Khasanov ³ Li Xiang ^{1,2} Sachith Dissanayake,⁴ Ritu Gupta,³ Masaaki Matsuda ⁴ Feng Ye,⁴ Bianca Haberl ⁴ Udhara Kaluarachchi,^{1,2} Robert J. McQueeney,^{1,2} Andreas Kreyssig,^{1,2} Sergey L. Bud'ko ^{1,2} and Paul C. Canfield^{1,2}

¹*Ames Laboratory, US Department of Energy, Iowa State University, Ames, Iowa 50011, USA*

²*Department of Physics and Astronomy, Iowa State University, Ames, Iowa 50011, USA*

³*Laboratory for Muon Spin Spectroscopy, Paul Scherrer Institute, 5232 Villigen PSI, Switzerland*

⁴*Neutron Scattering Division, Oak Ridge National Laboratory, 37830 Oak Ridge, Tennessee USA*



(Received 20 October 2020; revised 20 January 2021; accepted 22 January 2021; published 4 February 2021)

LaCrGe₃ has attracted attention as a paradigm example of the avoidance of ferromagnetic (FM) quantum criticality in an itinerant magnet. Here, we combined thermodynamic (specific heat and thermal expansion), transport, x-ray, and neutron scattering as well as μ SR measurements to obtain insights on the temperature-pressure phase diagram of LaCrGe₃. Consistent with previous studies of the phase diagram by transport measurements, our thermodynamic data shows clearly that the FM transition at T_{FM} changes its character from second order to first order when it is suppressed to low temperatures by pressure. In addition, previous studies demonstrated that for high pressures a new phase occurs below T_2 , which was proposed to be a long-wavelength antiferromagnetic state (AFM_q). In this paper, we provide evidence from our thermodynamic data that this phase transition is preceded by yet another phase transition at $T_1 > T_2$. Our μ SR data indicate that full magnetic volume fraction is only established below T_2 , but that this magnetism is characterized by a short correlation length. Within the experimental resolution, our neutron-scattering data is not able to identify any magnetic Bragg peaks. Overall, the microscopic magnetic data is therefore consistent with the formation of FM clusters in the proximity of the avoided FM quantum critical point in LaCrGe₃. This conclusion is at odds with the previous proposal of AFM_q order and raises questions on the role of disorder in this stoichiometric compound.

DOI: [10.1103/PhysRevB.103.075111](https://doi.org/10.1103/PhysRevB.103.075111)

I. INTRODUCTION

The fluctuations, associated with quantum-critical points (QCPs), i.e., second-order phase transitions at zero temperature (T), have been considered as crucial [1] for the stabilization of intriguing phenomena, such as superconductivity or non-Fermi liquid behavior [2]. This motivates the search for novel states by tuning a magnetic phase transition [3–13] to $T = 0$ K by external parameters, such as physical pressure, p , or chemical substitution. Whereas for antiferromagnetic (AFM) transitions, there is a large body of experimental evidence that a QCP can be accessed in metals, e.g., in heavy-fermion systems [14] or in iron-based superconductors [15], the ferromagnetic (FM) transition in clean, metallic magnets [16] is fundamentally different. Generic considerations [17–22] suggest that the QCP is avoided when a second-order paramagnetic (PM)-FM transition in a clean, metallic system is suppressed to lower T (with the exception of noncentrosymmetric metals with strong spin-orbit coupling [23]). The predicted outcomes are generally either (i) that the PM-FM transition becomes a first-order quantum-phase transition or (ii) that a new ground state, such as a long-wavelength AFM state (denoted by AFM_q) intervenes

the FM QCP. Experimentally, the first scenario was verified in a variety of systems [16,24–27], whereas the second scenario has so far been discussed for only a small number of systems. Among those are CeRuPO [28], PrPtAl [29], MnP [12], Nb_{1-y}Fe_{2+y} [30,31], LaCrGe₃ [32,33], and, very recently, La₅Co₂Ge₃ [34]. For understanding the avoided criticality in clean metallic FM systems, LaCrGe₃ [35] turns out to be an important reference system [32,33,35,36]. First, LaCrGe₃ is a simple $3d$ electron system with simple FM structure at ambient p . Second, the FM transition can be tuned by p to lower T . Thus, the tuning does not change the level of disorder in the system. Third, earlier studies [32,33] suggested that the FM transition in LaCrGe₃ becomes first order at a tricritical point [37,38] but also indicated the emergence of a new phase above ≈ 1.5 GPa. It was proposed that the new phase is likely the theoretically predicted AFM_q phase, but direct evidence by, e.g., neutron scattering was missing up to now.

Motivated by the need to identify the nature of the various phases in LaCrGe₃ across the avoided FM QCP region, we present an extensive study of thermodynamic, transport, x-ray diffraction, neutron scattering, and muon-spin resonance (μ SR) experiments. Consistent with previous studies, our thermodynamic data show that as the FM transition is monotonically suppressed with increasing p , the FM transition becomes first order at $p_{\text{tr}} \approx 1.5$ GPa. In addition, the thermodynamic data clearly demonstrate that two anomalies at T_1 and T_2 , that are very close in T with $T_1 > T_2$, emerge

*egati@iastate.edu

for higher p . The transition at T_1 has not been reported so far. This result implies the formation of multiple phases as an outcome of avoided FM criticality in this material. Our microscopic data show that for $T_2 < T < T_1$ the magnetic volume fraction is strongly T dependent and full volume fraction is only established below T_2 . At the same time, our results indicate that even below T_2 the magnetism is not consistent with long-range order. Together with the presence of a remanent magnetization, the data suggest the formation of short-range ordered FM clusters. These results therefore question the existence of a long-range ordered AFM_q phase emerging near the boundary of the first-order FM transition line in LaCrGe₃. Instead, the resulting phase diagram raises questions on the interplay of competing FM and AFM magnetic interactions and weak disorder close to the avoided FM QCP in LaCrGe₃.

II. EXPERIMENTAL METHODS

In the following, we provide an overview of the experimental methods and pressure environments used. More details for each technique can be found in Appendix A 1. Single crystals of LaCrGe₃ were synthesized using the solution-growth technique, as described in Ref. [35]. The obtained single crystals of rodlike shape were characterized by means of x-ray diffraction, resistance, and magnetization at ambient pressure prior to all measurements under pressure. The results of ambient-pressure characterization were consistent with previous reports [32,33,35] in terms of the Curie temperature T_{FM} as well as the residual resistivity ratio RRR .

Specific heat under pressure was measured using the ac calorimetry technique, as described in detail in Refs. [39,40]. Thermal expansion, i.e., the macroscopic length change of a crystal of LaCrGe₃ along a particular crystallographic axis as a function of temperature, was measured using strain gauges (after Ref. [41]). Resistance under pressure was measured in a linear four-point configuration with current directed along the crystallographic c axis (note that previously published data [32] were obtained with current in the ab plane). For all three measurements, the pressure environment was identical. Pressure up to ≈ 2.5 GPa was generated in a piston-cylinder double-wall pressure cell with the outer cylinder made out of grade 5 titanium alloy (Ti 6Al-4V) and the inner cylinder out of Ni-Cr-Al alloy (see Ref. [42] for a very similar design). We note that a pressure cell of the same design (with Be-Cu instead of Ti 6Al-4V outer cylinder) and same pressure medium were also used in previous studies of the T - p phase diagram in resistance measurements [32,33].

X-ray diffraction measurements under pressure were performed on single crystals and powder at station 6-ID-D and station 16-BM-D, respectively, of the Advanced Photon Source, Argonne National Laboratory. The samples were pressurized in diamond anvil cells (DACs) (part of the Diacell Bragg Series, Almax easyLab [43], 600- μ m culets) using steel gaskets and He gas as a pressure-transmitting medium.

Neutron-diffraction measurements were performed on single crystals using the HB1 diffractometer at the High Flux Isotope Reactor, Oak Ridge National Laboratory at ambient pressure (labeled as experiment N0) and finite pressures. For measurements with $p < 2$ GPa (experiment N1), a piston-cylinder cell was used, which is similar in design to the

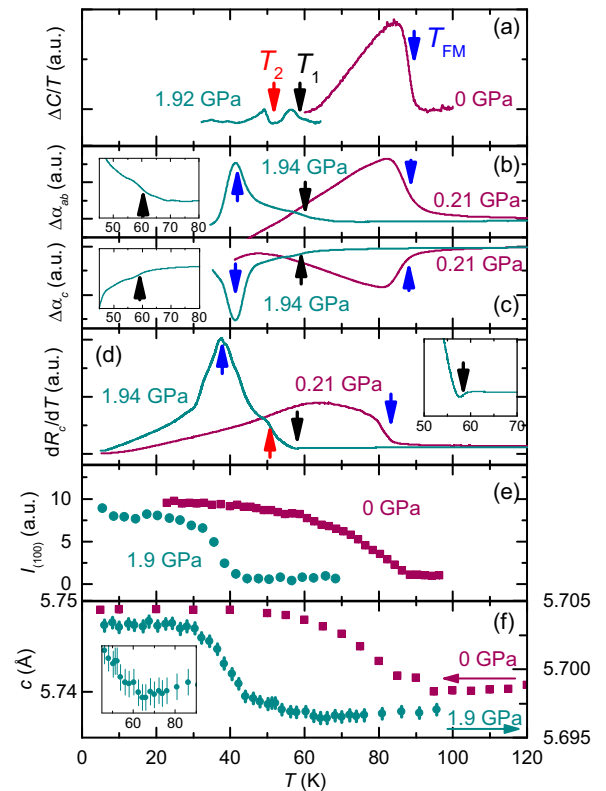


FIG. 1. Thermodynamic, transport, and diffraction data of LaCrGe₃ for low pressures (close to $p \approx 0$ GPa) and high pressures ($p \approx 1.9$ GPa) as a function of temperature, T . (a) Anomalous contribution to the specific heat, $\Delta C/T$. (b), (c) Anomalous contribution to the thermal expansion coefficient along the ab axes, α_{ab} , and the c axis, α_c . (d) T derivative of the resistance along the c axis, dR_c/dT . (e) Integrated intensity of the (1 0 0) neutron-diffraction Bragg peak (nuclear and magnetic contributions). (f) c axis lattice parameters from x-ray (0 GPa) and neutron (1.9 GPa, experiment N1) diffraction experiments. The arrows indicate the position of various anomalies at T_{FM} , T_1 , and T_2 . Insets in (b)–(d) and (f) show the high- p data sets on enlarged scales around T_1 .

one in Ref. [44]. For measurements with $p > 2$ GPa (experiment N2), a clamp-type palm cubic anvil cell (PCAC) was used with ZrO₂ anvils and a gasket made out of an Al-based alloy [45]. In addition, we also performed high-pressure elastic neutron-scattering measurements (experiment N3) in a DAC [46] (Versimax anvils, 3 mm culets, PH15-5 steel gasket, glycerin as pressure transmitting medium) using the time-of-flight diffractometer CORELLI at the Spallation Neutron Source, Oak Ridge National Laboratory.

Muon-spin resonance (μ SR) measurements under pressure were made on a large number of randomly oriented single crystals that were placed in a piston-cylinder pressure cell [47].

III. RESULTS

A. Emergence of new phase in the T - p phase diagram

Figure 1 shows representative data sets of the anomalous contribution to specific heat ($\Delta C/T$) (here the term anomalous indicates that data were corrected for a background

contribution, see Appendix A 2), the anomalous contribution to the thermal expansion coefficient ($\Delta\alpha_i$ with $i = ab, c$), the c axis resistance (R_c), the integrated neutron intensity of the (1 0 0) Bragg peak (I_{100}), and the c lattice parameter for $p < p_{tr}$ (represented by $p \approx 0 - 0.21$ GPa data) and $p > p_{tr}$ (represented by $p \approx 1.9$ GPa data).

For $p \approx 0 - 0.21$ GPa, we find clear anomalies at $T_{FM} \simeq 90$ K (see blue arrows) that are consistent with FM ordering with moments aligned along the c axis [35], as suggested by the increase of the I_{100} intensity. The mean-field-type thermodynamic signatures are consistent with a second-order phase transition. Notably, the transition is accompanied by sizable lattice changes, as evident from the evolution of α_i ($i = ab, c$) and the c lattice parameter. Specifically, the in-plane a axis (the out-of-plane c axis) decreases (increases) upon entering the FM state.

For $p \approx 1.9$ GPa, our collection of data shows anomalies at three characteristic temperatures. Upon cooling, a clear anomaly occurs in $\Delta C/T$ and dR_c/dT at $T_1 \simeq 60$ K, together with small but resolvable changes of the lattice in the a and c directions. Interestingly, the anisotropic response of the crystal lattice, α_{ab} and α_c , at T_1 is similar to the one at T_{FM} , albeit much smaller in size, i.e., we find a contraction (expansion) along the a (c) axis upon cooling through T_1 . At $T_2 \simeq 50$ K, another anomaly of similar size in $\Delta C/T$ is clearly resolvable, which, however, does not have any discernible effect in α_{ab} and α_c . Further cooling to $T_{FM} \simeq 40$ K results in a strong feature in α_i and the c lattice parameter, which, given the increase of I_{100} , is associated with the formation of long-range FM order, but does not result in a clear feature in $\Delta C/T$. In contrast to low p though, the symmetric and sharp shape of the anomaly in α_i for both directions is strongly reminiscent of a first-order phase transition (cf. also the more steplike change of c and I_{100} at T_{FM}). This, together with a sizable thermal hysteresis (see Appendix A 6), is clear thermodynamic evidence for the change of character of the FM transition from second order to first order at p_{tr} .

The positions of the various anomalies, which we inferred from the full T - p data sets up to ≈ 2.5 GPa (see Appendices A 2, A 3, and A 8), are compiled in the T - p phase diagram in Fig. 2. Upon suppressing T_{FM} with p , the FM transition changes its character from second order to first order at $(p_{tr}, T_{tr}) = [1.5(1) \text{ GPa}, 53(3) \text{ K}]$ (see Appendix A 6 for the determination of the position). For $p \gtrsim p_{tr}$, the anomalies at T_1 and T_2 emerge. (Only the latter phase line was identified in previous studies [32,33].) The T_1 and the T_2 lines do not only both emerge in immediate vicinity to (p_{tr}, T_{tr}) but also closely follow each other in the phase diagram and are suppressed much more slowly by p than T_{FM} . The latter observation suggests that the two anomalies are related. Altogether, this phase diagram highlights the complex behavior associated with the avoided FM QCP in LaCrGe₃.

The previous phase diagram, proposed in Refs. [32,33], included a crossover line from the FM state to a so-called FM2 state at lower pressures, as well as a so-labeled AFM_q phase at high pressures, when the FM transition line is fully suppressed. A detailed discussion of our data concerning the FM-FM2 crossover can be found in Appendix A 7. Since we were not able to find clear signatures of this crossover based on our thermodynamic, x-ray, and neutron data, we did not

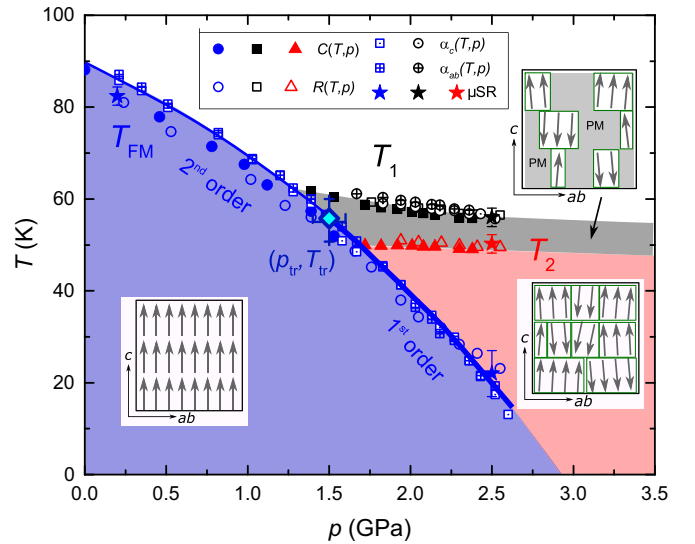


FIG. 2. Temperature-pressure (T - p) phase diagram of LaCrGe₃, constructed from specific heat, thermal expansion, resistance, and μ SR measurements, which are shown by different symbols. Lines are guides to the eyes. The blue-shaded region (delimited by the blue symbols at T_{FM}) corresponds to the region of ferromagnetic (FM) order, which is schematically depicted in the insets by spins (arrows) pointing along the crystallographic c axis. The rhombus marks the position of the tricritical point at (p_{tr}, T_{tr}) , at which the character of the FM transition changes from second order for low p to first order for high p . Dark grey and red-shaded regions correspond to new phases that occur for $p \gtrsim 1.5$ GPa. The insets visualize the suggested short-range-ordered phases in this p region. For $T_1 > T > T_2$, small clusters of varying size with FM order are embedded in a paramagnetic (PM) matrix. For $T < T_2$, these clusters fill the whole sample volume.

include any data points in our phase diagram. In addition, since we were not able to fully suppress the FM transition in our data by a pressure of 2.6 GPa, we do not have any data available on the proposed AFM_q. Last, based on our analysis, the tricritical point is located at slightly higher temperatures, closer to the previously reported Lifshitz point, than in the previous studies. Within the experimental error in the determination of the tricritical point, the position of the tricritical point here is not distinguishable from the intercept of the T_{FM} and T_1 or the T_{FM} and T_2 lines.

B. Microscopic study of magnetism: Absence of long-range magnetic order

To discuss the nature of the phases below T_1 and T_2 that are delineated in Fig. 2 by multiple thermodynamic and transport measurements, we turn to μ SR and neutron-scattering measurements under pressure. Previous μ SR measurements under p [32] showed a clear magnetic signal below ≈ 50 K at 2.3 GPa. To confirm this result and to refine the onset temperature, we performed another μ SR study with a finer T data-point spacing close to T_1 and T_2 at 2.55 GPa. Figure 3 shows selected μ SR spectra in (a) zero field (ZF) and (b) weak-transverse field (wTF). Both data are in full agreement with the notion of some type of local (on the scale of μ SR) magnetic order in the new phases, as evident from the observa-

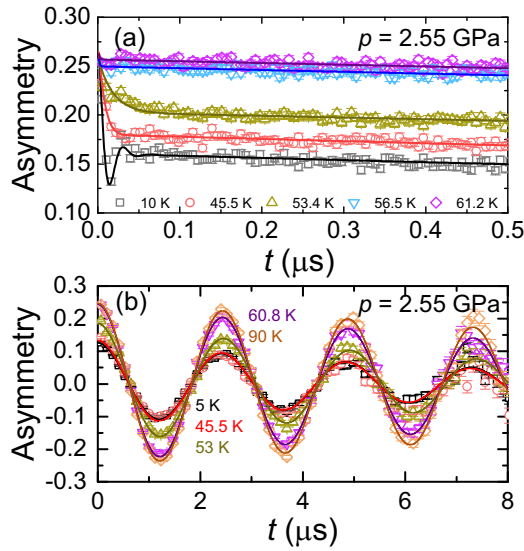


FIG. 3. μ SR spectra of LaCrGe_3 at $p = 2.55$ GPa: (a) Zero-field spectra for $10 \text{ K} \leq T \leq 61.2 \text{ K}$ at early response time, (b) weak-transverse field spectra for $5 \text{ K} \leq T \leq 90 \text{ K}$. In both panels, symbols correspond to the measured data, and solid lines correspond to fits by Eqs. (A5) and (A6) (see Appendix A 5 b).

tion of oscillations in the ZF data (a) as well as the additional damping in the wTF data in (b).

To discuss the μ SR data in more detail, we show in Fig. 4 the T dependence of the internal field, B_{int} , and the transverse relaxation rate, λ_T , as a measure of the width of the field distribution, from μ SR data measurements in ZF at $p = 2.55$ GPa. We also include the T dependence of the magnetic asymmetry, A_{mag} , as a measure of the magnetic volume fraction, as well as the relaxation rate of the pressure cell, λ_{PC} , as a measure of the field in the pressure cell that is created by a sample with macroscopic magnetization, from μ SR measurements in a wTF at the same p (see Appendix A 5 b for a detailed explanation of μ SR measurements in a pressure cell). The thermodynamic and transport data for similar p in Fig. 4 are used to determine the positions of $T_1 \approx 56 \text{ K}$ and $T_2 \approx 49 \text{ K}$ as well as $T_{\text{FM}} \approx 22 \text{ K}$. B_{int} sets in between T_2 and T_1 and increases upon cooling, with low T values similar to the ones in the FM state (see Appendix A 5 b for the analysis of our data set at zero pressure, which is consistent with the data from Ref. [32]). λ_T shows a strong increase upon cooling through T_1 . However, upon further cooling through T_2 , λ_T remains at a relatively high, finite value and decreases only slightly below T_{FM} . This is in contrast to the observations at low pressures, where λ_T decreases strongly upon cooling below the FM phase transition. A large λ_T implies a broad field distribution, characteristic for not-well-ordered systems [48]. A_{mag} indicates partial volume fraction for $T_2 < T < T_1$ and $A_{\text{mag}} \approx 0.12$ for $T \leq T_2$, consistent with full volume fraction (note that approximately half of the muons stop in the pressure cell). Last, λ_{PC} is small above T_1 and starts to increase just below T_1 upon cooling. Below T_2 , λ_{PC} is finite and almost T independent. A finite λ_{PC} implies that the sample exhibits a macroscopic magnetization, which might indicate the presence of some FM component.

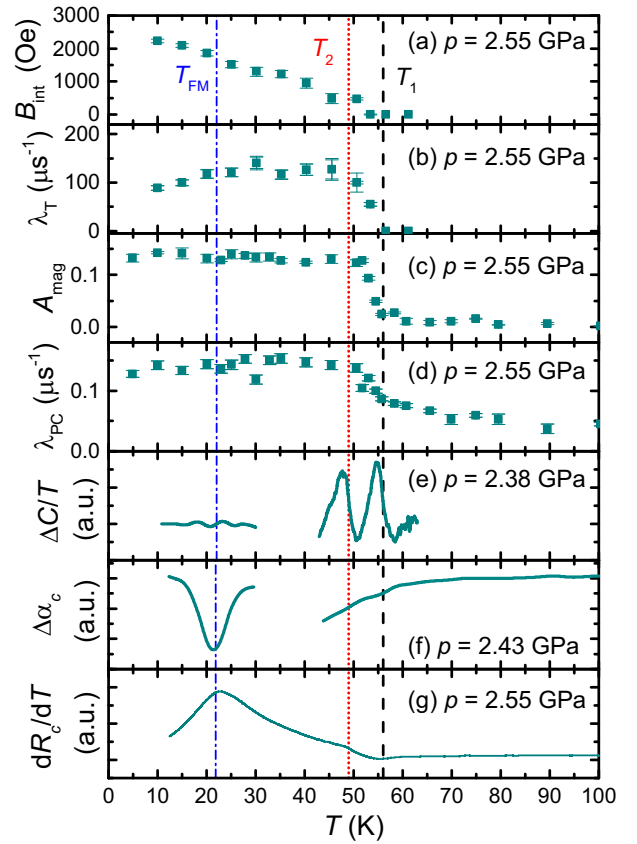


FIG. 4. Comparison of several high-pressure data sets close to a pressure, p , of 2.5 GPa as a function of temperature, T . (a)–(d) Internal field, B_{int} (a), transverse relaxation rate, λ_T (b), magnetic asymmetry, A_{mag} (c), and relaxation rate of the pressure cell, λ_{PC} (d), from zero field (a), (b) and weak transverse field (wTF) (c), (d) μ SR measurements at $p = 2.55$ GPa. (e) Anomalous contribution to specific heat, $\Delta C/T$ at $p = 2.38$ GPa. (f) Anomalous contribution to thermal expansion coefficient along the c axis, $\Delta\alpha_c$ at $p = 2.43$ GPa. The low- T and high- T data are plotted on different scales for a better visualization of the features. (g) T derivative of the resistance along the c axis, dR_c/dT , at $p = 2.55$ GPa. Black dashed, red dotted, and blue dashed-dotted lines indicate the position of the anomalies at T_1 , T_2 , and T_{FM} , respectively.

To further underline this finding, we also searched for the presence of a remanent magnetization in the μ SR experiment, since any remanent magnetization of the sample is expected to distort the μ SR signal from the pressure cell. To this end, we compared the ZF μ SR spectra before and after the application of a magnetic field of 6000 Oe. These two spectra are shown in Figs. 5(a)–5(c) for 5 K, 35 K, and 60 K. According to our phase diagram (see Fig. 2), LaCrGe_3 is in the FM phase at 5 K [Fig. 2(a)], in the T_2 phase at 35 K [Fig. 2(b)], and in the high-temperature PM phase at 60 K [Fig. 2(c)]. The raw data already indicate that for $T = 5 \text{ K}$ and 35 K, the muon-time spectrum after the application of field is different from the initial time spectrum. In contrast, at $T = 60 \text{ K}$, the ZF time spectrum after the application of field is almost unmodified from the initial ZF time spectrum. A quantitative analysis of this behavior is obtained from considering the evolution of the fit parameter λ_{PC} with temperature and magnetic field, which

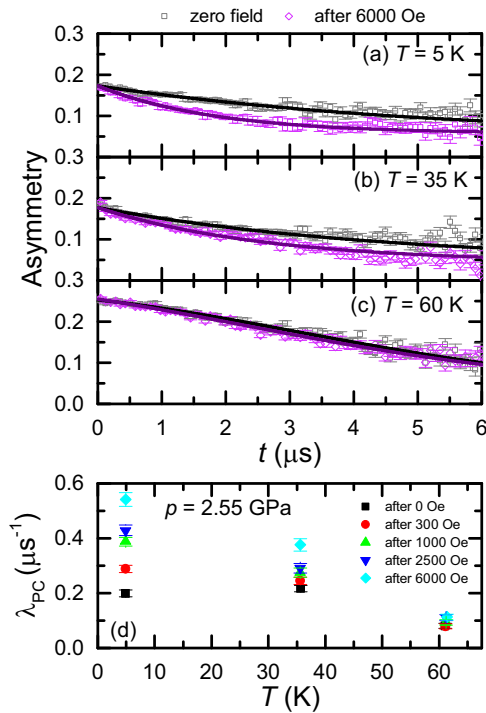


FIG. 5. Search for remanent magnetization in μ SR measurements under pressure. (a)–(c) Initial zero-field μ SR time spectra and zero-field spectra after increasing and decreasing the magnetic field to 6000 Oe (symbols) at $T = 5$ K (a), 35 K (b), and 60 K (c) at $p = 2.55$ GPa. Solid lines are fits to the experimental data by Eq. (A9). (d) Pressure-cell relaxation rate, λ_{PC} , as a function of temperature, T , at $p = 2.55$ GPa. λ_{PC} was extracted from fitting the experimental data. A clear change of λ_{PC} after application of a field can be observed for 5 K and 35 K, whereas there is no change within the experimental resolution for 60 K.

is shown in Fig. 5(d). We note that the λ_{PC} values obtained here from ZF experiments are usually larger by a factor of ≈ 1.8 than those λ_{PC} values obtained in wTF experiments [48] (shown in Fig. 4). Whereas the ZF λ_{PC} is small for 60 K and almost independent of field, λ_{PC} is clearly larger and stronger field dependent for 35 K and 5 K. This all suggests that for 5 K and 35 K there exists a remanent magnetization, in particular, also for the T_2 phase. Due to lower statistics, this response was not detected in the previous μ SR study [32] and it clearly calls into question the notion of AFM $_q$ order in the new phase.

To complement our microscopic study of the magnetism in the high-pressure phases, we now turn to the results of our neutron-diffraction study. First, we focus on the evolution of the (1 0 0) Bragg peak, which is sensitive to the FM order. In Fig. 6, we compare the (1 0 0) Bragg peak in neutron diffraction for selected T at $p = 1.9$ GPa. A clear (1 0 0) Bragg peak is observed in the PM state ($T = 68$ K) corresponding to the nuclear contribution, and grows markedly below $T_{FM} \simeq 40$ K (at $T = 38$ K and 6 K) due to the FM contribution. The moment in the FM ground state is $1.4(3) \mu_B$, which was determined from the intensity of the (1 0 0) Bragg peak relative to a set of nuclear Bragg peaks. For $T_{FM} < T < T_2$, shown here by the 44 K data, the (1 0 0) Bragg peak is not distinguishable from the data in the PM phase [see also

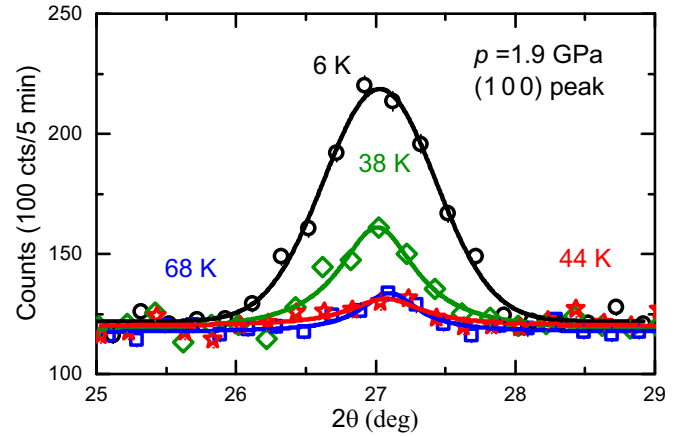


FIG. 6. Neutron studies of ferromagnetism in LaCrGe₃ under pressure: Angle-dependent neutron intensity around the (1 0 0) Bragg peak at a pressure $p = 1.9$ GPa for different temperatures. Lines are guide to the eyes. Data were taken in experiment N1.

Fig. 1(e)]. Based on this result (and results at higher pressures, see Appendix A 5 a), we can thus exclude long-range FM order below T_1 and T_2 with a moment larger than $0.4 \mu_B$.

Furthermore, for a study of the magnetic nature of the high-pressure phases, we also surveyed large sections of reciprocal space for additional magnetic peaks using CORELLI at $p = 3.5$ GPa (see Appendix A 5 a for selected scans along high-symmetry directions taken at HB1 at $p = 1.9$ GPa, 2.5 GPa, and 3.5 GPa). For this pressure of 3.5 GPa, the phase diagram from Ref. [32] clearly indicates the presence of the new magnetic phase below ≈ 50 K. In Fig. 7, we show 2D images of the (H K 0), (H H 0), and (H 0 L) reciprocal planes at $T = 5$ K [Figs. 7(a), 7(c) and 7(e)] and 30 K [Figs. 7(b), 7(d) and 7(f)]. Nuclear Bragg peaks from LaCrGe₃ are clearly seen alongside the rings from the polycrystalline steel gasket. However, no superstructure peaks, indicative of any AFM magnetic order, were found in our experiment. Thus, we can also exclude any type modulated AFM order below T_1 and T_2 , i.e., the previously suggested AFM $_q$ -type magnetic order [32] within our experimental resolution. For a c -axis modulated AFM order, as assumed in the DFT calculations of Ref. [32], we would have been able to detect long-range order with a moment larger than $0.7 \mu_B$. In addition, we can rule out the formation of a charge-density wave or structural transition at high p from x-ray diffraction studies (see Appendix A 4).

IV. DISCUSSION

We now turn to a discussion of the nature of the p -induced phases that emerge for $p \gtrsim p_{tr}$ and $T \lesssim T_{tr}$. We start by focusing on the range $T < T_2$, for which the μ SR data suggest $\approx 100\%$ volume fraction, but no magnetic Bragg peak could be resolved in neutron-diffraction experiments. Given that the μ SR data indicate a similar B_{int} for the low- p FM state and the new phase below T_2 at low T , it seems unlikely that the moment of the T_2 phase is so low that it falls below our sensitivity in neutron measurements. Following this argument, an obvious scenario, which would reconcile both μ SR and neutron results, would be that the magnetic order below T_2

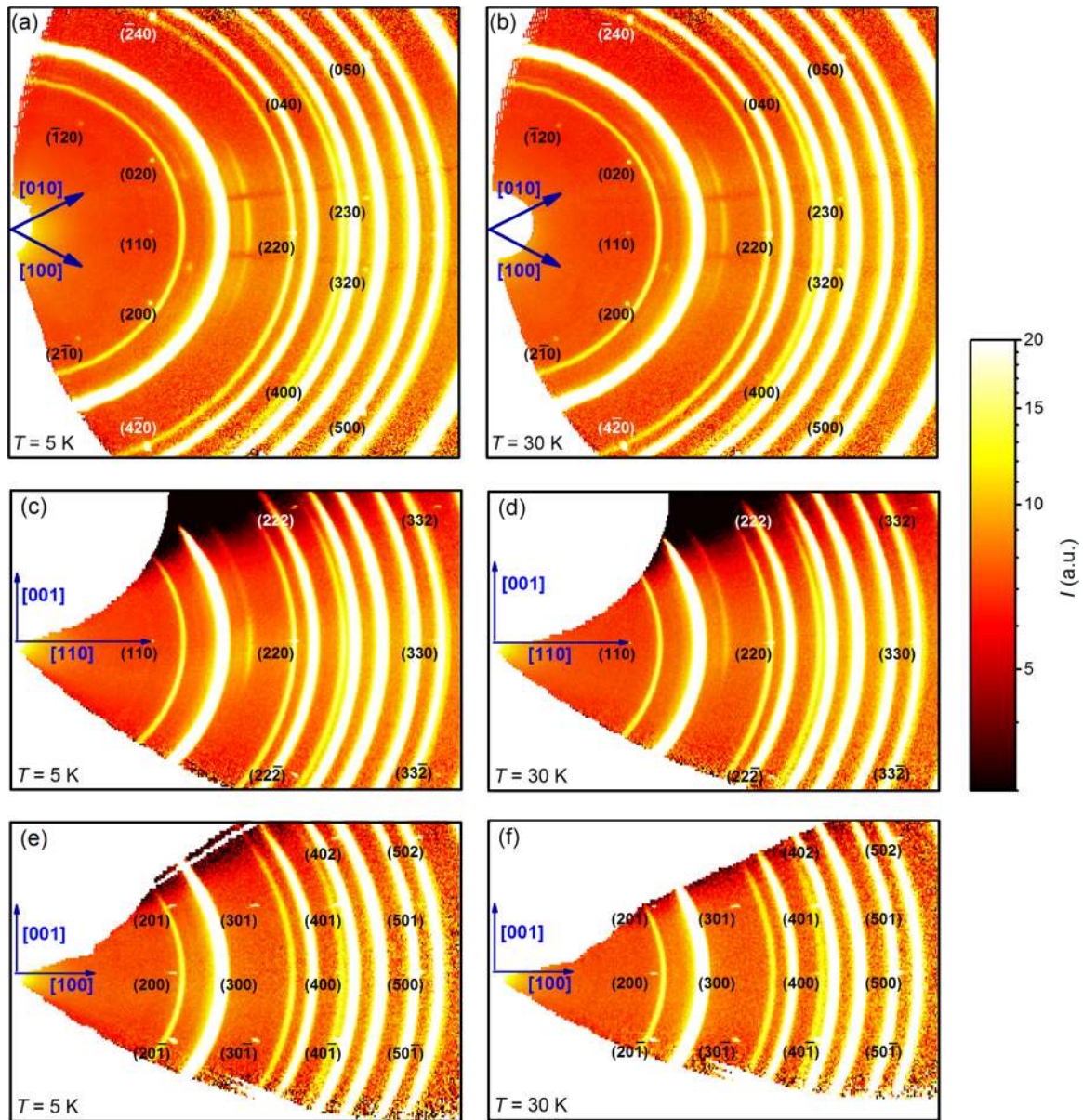


FIG. 7. Neutron studies of the entire q space for high pressures: Several slices of neutron-diffraction data taken at CORELLI of a LaCrGe_3 single crystal in a DAC with $p = 3.2$ GPa. For each panel, nuclear Bragg peaks are indicated in black or white text and the reciprocal space direction of the crystal is indicated in blue with arrows. Polycrystalline rings are from the steel gasket with strong intensity modulation arising from the texture and strain in the gasket. Cuts of the neutron data are shown for the $(H K 0)$ plane (a), (b); $(H H L)$ plane (c), (d); and $(H 0 L)$ plane (e), (f) at two temperatures, $T = 5$ K (a), (c), (e) and 30 K (b), (d), (f). Data were taken in experiment N3.

is only short range. We note that the sizable λ_T value for $T < T_2$ is fully consistent with the notion of a short-range ordered state [48] in which magnetic clusters exist. To discuss the question whether the order within these clusters is FM or AFM, we refer to the observations of a finite λ_{PC} and a remanent magnetization below T_2 from μSR . This speaks in favor of FM order in each cluster, whereas the clusters might either align FM or AFM with respect to each other (see inset of Fig. 2 for a schematic picture). We speculate that at least some of the clusters align AFM with respect to each other, since this would naturally explain the small but finite λ_{PC} . An estimation of the size of such FM clusters can be inferred from the λ_T value as well as the data of the $(1\ 0\ 0)$ Bragg peak. The

large value of λ_T between T_2 and T_{FM} yields an estimate for the cluster size of 6 nm [48]. For the neutron data, when we assume a similar moment size as in the FM state, as suggested by a similar B_{int} , the absence of a clear magnetic $(1\ 0\ 0)$ Bragg peak results in an estimate of the average cluster size of less than 12 nm. Note that we cannot distinguish experimentally between clusters of uniform or varying size, and that moment size and average cluster size can change with decreasing T , as suggested by a continuous change of B_{int} , the c lattice parameter and α_i .

How is LaCrGe_3 for $T_2 < T < T_1$ then characterized? Our results indicate that in this regime the magnetic volume fraction is strongly T dependent and increases from ≈ 0 at T_1

upon cooling to $\approx 100\%$ at T_2 . We also recall our result of the lattice strain: (i) the lattice response upon cooling through T_1 shows the same sign of the directional anisotropy as for the FM transition, but only smaller in size, i.e., the lattice shrinks (expands) along the a (c) axis at T_1 as well as T_{FM} and (ii) there are no pronounced lattice effects at T_2 . The latter result might indicate that no strong modification of the magnetic order occurs at T_2 , since it would likely result in an additional lattice strain. It thus appears likely that the magnetic clusters start to form in the range $T_2 < T < T_1$ and either their number or size is strongly dependent on T (see inset of Fig. 2). The size and anisotropy of the observed lattice strains would be consistent with the notion of small FM clusters, in which moments are primarily aligned along the c axis (a small tilt away from the c axis is possible) and in which the partial AFM alignment of the clusters with respect to each other strongly reduces the lattice strain (in contrast to large FM domains in the low- p FM state, resulting in large strains). We want to clearly point out that the scenario proposed above only gives rise to two specific heat features if the increase in magnetic volume fraction is stronger close to the phase transitions at T_1 and T_2 than in between T_1 and T_2 . However, the two specific-heat features might also imply an alternative scenario in which the phase for $T_2 < T < T_1$ corresponds to a different type of magnetic or structural order [49,50]. Our structural investigations (see Appendix A 4) did not indicate any lattice symmetry change across the entire T range for high p and, again, μSR measurements do not indicate full volume fraction in this temperature range. A quest for further clarification on the nature of this intermediate T phase should motivate future theoretical and experimental investigations.

Our main results on the avoidance of FM criticality in the itinerant magnet LaCrGe_3 can be summarized as follows. First, consistent with previous studies, our thermodynamic data provided evidence for a change of the transition character from second order to first order, typically considered a hallmark for the avoidance of the QCP in clean metallic FM systems. Second, we argued that short-range magnetic phases rather than long-wavelength AFM order [32] exist for $p \geq p_{\text{tr}}$ between T_1 and T_{FM} , which is usually associated with the effects of strong disorder [16]. The main question is then what drives the formation of short-range order in LaCrGe_3 : Do the enhanced AFM interactions, that are suggested by theory [17,19,21,49,51,52], and the associated frustration between FM and AFM interactions lead to a tendency toward short-range order or does weak disorder promote short-range order? In fact, an earlier theoretical study [51] pointed out that the tricritical point can survive up to a critical disorder strength, whereas an amount of disorder smaller than the critical disorder strength can cause a short-range spiral state. So far, this scenario has only been considered to be realized in the stoichiometric compound CeFePO [16,53], for which the interpretation is complicated by Kondo physics, and a tuning across the avoided QCP is lacking up to now. Interestingly, CeFePO and LaCrGe_3 have a very similar residual resistivity ratio [16,32] of ≈ 5 –10, which is lower than for other clean itinerant FM systems and might indicate a somewhat larger level of disorder. Overall, our results raise questions on the role of disorder in this itinerant magnet and motivate inves-

tigations of the T - p phase diagram with varying levels of disorder in the future.

V. CONCLUSIONS

In this paper, we combined thermodynamic, transport, and microscopic magnetic probes to study the avoided FM quantum criticality in LaCrGe_3 . Consistent with previous studies, we find that the FM transition becomes suppressed with pressure and changes its character from second order to first order above a critical pressure $p_{\text{tr}} \approx 1.5$ GPa. For high pressures, it was reported previously that a new type of magnetic order emerges below T_2 . We not only found thermodynamic signatures associated with this transition but also an additional transition at $T_1 > T_2$. This result illustrates further complexity of the phase diagram of LaCrGe_3 . Our microscopic μSR and neutron studies addressed the nature of the high-pressure phases. Whereas the μSR measurements indicated full magnetic volume fraction only below T_2 , the neutron data did not show any Bragg peak corresponding to long-range magnetic order below T_2 . Thus, our results are at odds with the previous proposal of long-wavelength AFM order at high pressures in LaCrGe_3 and instead point toward the formation of short-range magnetic phases, which are likely characterized by FM clusters. Correspondingly, these results then raise questions on the role of disorder in this stoichiometric compound for the outcome of avoided FM criticality.

ACKNOWLEDGMENTS

We thank A.I. Goldman, V. Taufour, and D.H. Ryan for useful discussions and S. Downing and C. Abel for the growth of single crystals. The authors would like to acknowledge B. Li, D. S. Robinson, C. Kenney-Benson, S. Tkachev, M. Baldini, S. G. Sinogeikin, and D. Popov for their assistance during the x-ray diffraction experiments. We thank C. Tulk, A. M. dos Santos, J. Molaison, and R. Boehler for support of the high-pressure neutron-diffraction study and Y. Uwatoko for providing us the palm cubic pressure cell. Work at the Ames Laboratory was supported by the U.S. Department of Energy, Office of Science, Basic Energy Sciences, Materials Sciences and Engineering Division. The Ames Laboratory is operated for the U.S. Department of Energy by Iowa State University under Contract No. DEAC02-07CH11358. E.G. and L.X. were funded, in part, by the Gordon and Betty Moore Foundation's EPIQS Initiative through Grant No. GBMF4411. In addition, L.X. was funded, in part, by the W. M. Keck Foundation. A portion of this research used resources at the High Flux Isotope Reactor and the Spallation Neutron Source, U.S. DOE Office of Science User Facilities operated by the Oak Ridge National Laboratory. This research used resources of the Advanced Photon Source, a U.S. DOE Office of Science User Facility operated for the US DOE Office of Science by Argonne National Laboratory under Contract No. DE-ac02-06CH11357. We gratefully acknowledge support by HPCAT (Sector 16), Advanced Photon Source (APS), Argonne National Laboratory. HPCAT operations are supported by DOE-NNSA under Grant No. DE-NA0001974, with partial instrumentation funding by NSF. Use of the COMPRES-GSECARS gas loading system was supported by

COMPRES under NSF Cooperative Agreement Grant No. EAR-11-57758 and by GSECARS through NSF Grant No. EAR-1128799 and DOE Grant No. DE-FG02-94ER14466. Research of R.G. is supported by the Swiss National Science Foundation (SNF-Grant No. 200021-175935).

APPENDIX

1. Details of the experimental methods

a. Specific heat measurements under pressure

Specific heat under pressure was measured using the ac calorimetry technique, as described in detail in Refs. [39,40]. To this end, a single crystal of LaCrGe_3 was placed between a heater and a thermometer. The heater was supplied with an oscillating voltage and the resulting temperature oscillation of the sample, which is related to the specific heat of the sample, was recorded. Given the nonadiabatic conditions of the pressure-cell environment, absolute values of the specific heat cannot be obtained with high accuracy; nonetheless, the technique of ac calorimetry allows for a decoupling of the sample from the bath (i.e., the pressure medium and the cell), to a good approximation, by choosing the appropriate measurement frequency (see Ref. [39] for details on the procedure of the determination of the measurement frequency). Thus, changes of the specific heat with pressure can be obtained reliably. Our implementation of this technique [39] has proven to be particularly sensitive for the detection of specific-heat anomalies of varying size, resulting from different amounts of removed entropy and over a wide range of phase transition temperatures. This is highly beneficial for the present study, where the pronounced specific-heat anomaly at high temperatures close to 90 K at ambient pressure becomes suppressed to very low temperatures and strongly reduced in size.

The cryogenic environment was provided by a closed-cycle cryostat (Janis SHI-950 with a base temperature of ≈ 3.5 K). Pressure was generated in a piston-cylinder double-wall pressure cell with the outer cylinder made out of grade 5 titanium alloy (Ti 6Al-4V) and the inner cylinder out of Ni-Cr-Al alloy (see Ref. [42] for a very similar design). A mixture of 4:6 light mineral oil:n-pentane was used as a pressure-transmitting medium. It solidifies at $p \approx 3 - 4$ GPa at room temperature [54], thus ensuring hydrostatic pressure application over the available pressure range. Pressure at low temperatures was determined from the shift of the superconducting transition temperature of elemental lead (Pb) [55], which was determined in resistance measurements. The error in the determination of the low-temperature pressure is estimated to be 0.01 GPa, and pressure changes in this particular cell [56] by less than 0.04 GPa by increasing temperature up to 100 K.

b. Thermal expansion measurements under pressure

Thermal expansion, i.e., the macroscopic length change of a crystal of LaCrGe_3 along a particular crystallographic axis as a function of temperature, was measured using strain gauges, which are sensors whose resistance, R , changes upon compression or tension. For our measurements, strain gauges (type FLG-02-23, Tokyo Sokki Kenkyujo Co., Ltd. with $R \approx 120 \Omega$) were fixed rigidly to the sample by using Devcon 5 Minute Epoxy (No. 14250), and the resulting resistance

changes of the strain gauges were recorded and converted into length changes using the known gauge factor. In total, two strain gauges were fixed orthogonally on the same sample to measure the expansion along the ab axes and the c axis simultaneously. Since the strain gauge resistance varies not only due to the expansion of the crystal with temperature, but also due to the intrinsic resistance change of the strain gauge wire material, another set of strain gauges was mounted on a sample of general purpose grade C2 tungsten carbide (6% Co binder, fine grain size). Given that tungsten carbide is a very hard material and has a comparatively small expansion coefficient over a wide temperature range and, in particular, no anomalous behavior [57], the resistances of the strain gauges mounted on tungsten carbide are used to subtract the intrinsic resistance change of the strain gauge from the measured resistance data on LaCrGe_3 . This subtraction was performed *in situ* by using two Wheatstone bridges (see, e.g., Ref. [41] for similar designs). To this end, in each bridge, one strain gauge on the sample, one strain gauge on tungsten carbide inside the cell, and two thin-film resistors with similar and almost temperature-independent absolute resistances of $\approx 120 \Omega$, which were placed outside of the cell in the low- T environment, were used. The current for the bridge was supplied by a LakeShore 370 Resistance Bridge, which was also used to measure the voltage across each bridge. The cryogenic environment, pressure cell, pressure medium, and manometer were identical to the one for specific-heat measurements, see above.

c. Resistance measurements under pressure

Resistance under pressure was measured in a linear four-point configuration with current directed along the crystallographic c axis. Contacts were made using Epo-tek H20E silver epoxy. The ac resistance was measured by a LakeShore 370 Resistance Bridge.

d. High-energy x-ray diffraction measurements on single crystals under pressure

High-energy (100 keV) x-ray diffraction measurements were performed on single crystals at station 6-ID-D of the Advanced Photon Source, Argonne National Laboratory. The samples were pressurized in DACs (part of the Diacell Bragg Series, Almax easyLab [43]) using He gas as a pressure-transmitting medium. We used diamond anvils with 600 μm culets and stainless-steel gaskets preindented to thicknesses of $\approx 60 \mu\text{m}$, with laser-drilled holes of diameter $\approx 310 \mu\text{m}$. The wavelength of a fluorescence line of ruby was used for room-temperature pressure calibration. By measuring the lattice parameter of polycrystalline silver, we determined pressure *in situ* at all temperatures and pressures with an accuracy of 0.1 GPa. Large regions of the $(H H L)$ plane and the powder diffraction pattern of silver were recorded by a MAR345 image plate positioned 1.249 m behind the DAC while the DAC was rocked 2.4° along two independent axes perpendicular to the incident x-ray beam. At ambient pressure, other planes of high-symmetry were also recorded outside of a DAC. In addition, at ambient pressure, high-resolution measurements were taken of the Bragg peaks (16 0 0) and (0 0 16) with a Pixirad-1 detector positioned 1.210 m behind

the sample while rocking around one axis perpendicular to the incident x-ray beam.

e. Powder x-ray scattering measurements under pressure

Powder x-ray diffraction measurements were performed under pressure with 30 keV x rays at station 16-BM-D of the Advanced Photon Source, Argonne National Laboratory. The powder was made by crushing single crystals of LaCrGe_3 and only powder of less than a micron size was loaded into the DAC (Diacell Bragg Series, Almax easyLab [43]). The DAC was configured identically to the high-energy x-ray experiment described above with He gas as the pressure-transmitting medium, but the wavelength of a ruby fluorescence line was used to measure pressure at all temperatures and pressures with an accuracy of 0.1 GPa. Large regions of reciprocal space were recorded on a MAR345 image plate positioned 0.412 m behind the DAC. Individual crystallites of LaCrGe_3 still had very sharp peaks and so the sample was rocked along one axis perpendicular to the beam to obtain a better powder average.

f. Neutron-diffraction measurements at HB1 on single crystals at ambient and finite pressure

Neutron-diffraction measurements were performed on single crystals using the HB1 diffractometer at the High Flux Isotope Reactor, Oak Ridge National Laboratory. For measurements taken at ambient pressure, a single crystal was sealed in an Al can containing He exchange gas, which was then attached to the head of a He closed-cycle refrigerator (CCR). We refer to this experiment as N0. The beam collimators placed before the monochromator, between the monochromator and the sample, between the sample and analyzer, and between the analyzer and detector were $48^\circ-80^\circ-80^\circ-240^\circ$, respectively. HB1 operates at a fixed incident energy of 13.5 meV and contamination from higher harmonics in the incident beam was eliminated using pyrolytic graphite filters.

For measurements with $p < 2$ GPa, a piston-cylinder cell was used, which is similar in design to the one in Ref. [44]. We refer to these experiments throughout the text as N1. It was loaded with a single crystal placed within a Teflon capsule with Daphne 7373 as the pressure-transmitting medium, which solidifies at 2.5 GPa [54] at room temperature. For the 1.9 GPa measurement, the sample was loaded together with a NaCl single crystal, which was used to measure the pressure within the cell based on the lattice parameter changes before and after applying pressure at room temperature with an accuracy of 0.1 GPa. For all other pressures, the pressure was determined with an accuracy of 0.2 GPa based on a calibrated pressure-load curve measured at room temperature for that specific cell and was corrected for temperature-induced reduction of pressure via previous calibration measurements. We note that a different crystal was used for the 1.9 GPa measurements than for the other piston-cylinder cell experiments. The cell was then attached directly to the head of a CCR.

For measurements with $p > 2$ GPa, a clamp-type PCAC was used with ZrO_2 anvils and a gasket made out of an Al-based alloy [45]. We refer to these experiments throughout the text as N2. A single crystal with volume of $0.9 \times 0.9 \times$

1.5 mm^3 was attached to the bottom of a Teflon capsule together with a 1:1 mixture of Fluorinet FC70 and FC77 as the pressure-transmitting medium. Although this medium solidifies close to 1.1 GPa at room temperature, previous studies have shown that the PCAC applies pressure almost hydrostatically up to much higher pressures than the solidification pressure due to the three-dimensional anvil design [45] that allows us to compress the medium simultaneously along three orthogonal directions. The pressure was determined with an accuracy of 0.3 GPa at room temperature based on a calibrated pressure-load curve for that specific cell and was corrected for temperature-induced reduction of pressure via previous calibration measurements. After applying pressure, the cell was then loaded into a high-capacity CCR with a base temperature of approximately 3 K.

g. Neutron elastic-scattering measurements at CORELLI under pressure

Elastic-scattering measurements using a DAC [46] were performed using the time-of-flight diffractometer CORELLI at the Spallation Neutron Source, Oak Ridge National Laboratory. We refer to these experiments throughout the text as N3. CORELLI allows for the simultaneous measurement of large sections of the three-dimensional reciprocal space by utilizing a white-beam Laue technique with energy discrimination by modulating the incident beam with a statistical chopper [58]. This allows CORELLI to efficiently separate the elastic and inelastic channels of the diffuse scattering signal, thus identifying whether the observed correlation is static or not. By applying pressure in a DAC at CORELLI, we were able to reach pressures from 0.8 GPa to 3.2 GPa at base temperature of $T \approx 3$ K. DACs with single-crystal diamond anvils are heavily used for diffraction at the synchrotron, but to be used for neutron diffraction the DAC at CORELLI utilizes polycrystalline Versimax diamond anvils [59]. Measurements of MnP have shown that CORELLI is capable of measuring moments as low as $0.25 \mu_B/\text{Mn}$ within a DAC [59]. The sample (sample thickness of $\approx 210 \mu\text{m}$ and sample cross-sectional area of $0.7 \times 0.7 \text{ mm}^2$) was loaded onto one polycrystalline anvil with the PH15-5 steel gasket (500 μm height, 3 mm culet size, 1.3 mm initial gasket hole) in place with deuterated glycerin as a pressure medium, which solidifies at ≈ 5 GPa at room temperature [60] but remains soft, providing close to hydrostatic conditions up to 9 GPa [61]. This was then sealed and pressurized at room temperature with a press. Note that an initial experiment using 4:1 methanol:ethanol as a pressure-transmitting medium did not succeed because the pressure medium evaporated too quickly during sealing. In contrast, glycerin does not readily evaporate in air, which ensures that the pressure-transmitting medium is contained. Pressure was assigned to the one obtained from a calibrated pressure-load curve for that specific cell and anvil/gasket setup at room temperature with an accuracy of 0.5 GPa. After applying pressure, the cell was then attached onto the head of a CCR. We took measurements with the well-focused incident beam passing through the steel gasket from the side. Both gasket and Versimax anvils only yield powder-diffraction rings, which can be readily distinguished from the single-crystal sample peaks.

h. μ SR measurements under pressure

Approximately 100 small single crystals of LaCrGe_3 (in total ≈ 2 g) from three batches were placed inside a double-wall piston-cylinder cell. Care was taken to ensure as high of a filling factor of the sample space as possible, as well as to ensure a random orientation of the small single crystals. Both the inner and the outer cylinder of the pressure cell, which was specially designed for use in μ SR experiments, are made out of MP35N alloy [47]. The maximum pressure of this cell is ≈ 2.5 GPa. Daphne 7373 oil was used as a pressure-transmitting medium, which solidifies at room temperature close to 2.5 GPa [54]. The pressure at low temperatures was determined from the shift of the superconducting transition of elemental indium [62], which was also placed in the pressure cell. We estimate the error in this low-temperature pressure to be ≈ 0.05 GPa. The superconducting transition temperature of indium was determined in ac susceptibility measurements prior to the μ SR experiments in a separate ^4He cryostat. In total, μ SR measurements were performed in zero magnetic field and in several transverse magnetic fields (up to 6000 Oe) at 0.2 GPa as well as at the maximum pressure of 2.5 GPa. The measurements were performed in a ^4He cryostat with base temperature of 2.2 K at the μE1 beamline at the Paul-Scherrer-Institute in Villigen, Switzerland, by using the GPD spectrometer. Typically, $5 - 10 \times 10^6$ positron events were counted for each data point.

i. Pressure media and homogeneity

For all experiments under finite pressure, the pressure media and cell design was chosen such to ensure hydrostatic or close to hydrostatic pressure conditions in the pressure range of interest [45,54,59,61,63,64].

2. Specific-heat data under pressure

a. Specific-heat data sets under pressure and procedure to obtain anomalous specific-heat contributions

Figure 8 shows selected data sets of specific heat divided by temperature, C/T , which were taken during this study, covering the pressure range $0.46 \text{ GPa} \leq p \leq 2.38 \text{ GPa}$ and temperature range $5 \text{ K} \leq T \leq 100 \text{ K}$. These data sets were used to extract the anomalous contributions to the specific heat, i.e., the specific-heat data corrected for an estimate of the background contribution, resulting from, e.g., phonons. A previous work [35] demonstrated by comparison to the specific heat of nonmagnetic analog LaVGe_3 that the specific heat of LaCrGe_3 is dominated by nonmagnetic contributions at low temperatures and at temperatures higher than the FM transition at ambient pressure. Only close to the FM phase transition, a substantial magnetic contribution to specific heat was observed. Given that the ac specific heat technique used here does not allow us to determine specific-heat values to very high accuracy, we do not refer to specific-heat measurements of LaVGe_3 for the background subtraction for the LaCrGe_3 data under pressure (shown in Fig. 8), and instead follow the procedure, which is illustrated in Fig. 9 for a subset of the data. Following the outcome of the ambient-pressure study, we approximate the nonmagnetic background contribution by fitting the C/T data to a polynomial function of

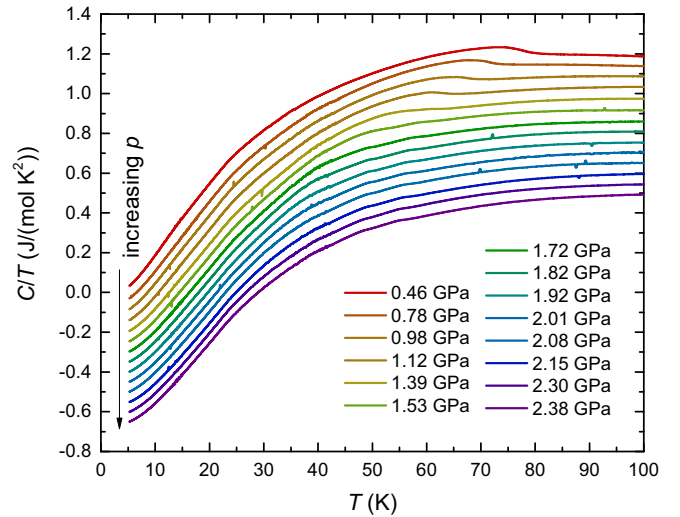


FIG. 8. Specific heat divided by temperature, C/T , of LaCrGe_3 versus T over a wide temperature range ($5 \text{ K} \leq T \leq 100 \text{ K}$) for finite pressures ($0.46 \text{ GPa} \leq p \leq 2.38 \text{ GPa}$). Data have been shifted vertically by $0.1 \text{ J}/(\text{mol K}^2)$ for clarity.

the order of three across a wide temperature range except in the immediate vicinity of any phase transition temperature T_p (i.e., either T_{FM} , T_1 , or T_2). Typically, the range $T_p - 10 \text{ K} \leq T \leq T_p + 5 \text{ K}$ was excluded from the fit and, overall, the fit was typically performed down to $T_p - 20 \text{ K}$ and up to $T_p + 20 \text{ K}$. The so-obtained background curves manifest a shoulder in C/T at $T \approx 80 \text{ K}$, which can also be seen in the ambient-pressure specific-heat data on LaVGe_3 when replotted as C/T versus T [35]. Note that this procedure of background subtraction leads to significant uncertainties in estimating the absolute size of specific heat (and thus entropy) that is associated with each phase transition. However, the conclusions, which are presented in the main text, are solely based on the analysis of the positions of anomalies in $\Delta C/T$,

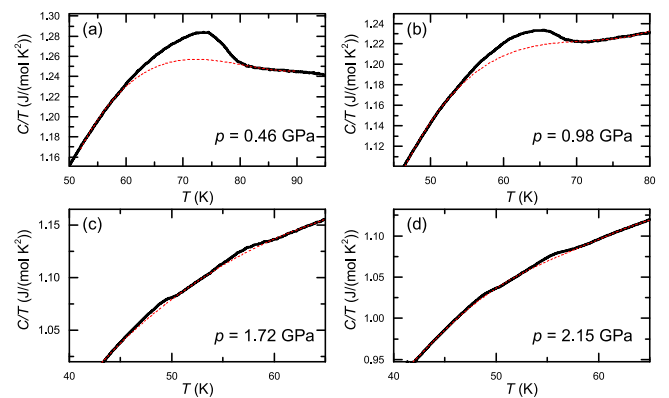


FIG. 9. Illustration of the procedure to obtain the anomalous specific heat contributions that are associated with various phase transitions in LaCrGe_3 for selected pressures (a)–(d). The background (red dashed line) was obtained by fitting the specific-heat data (black line) well below and well above the phase transitions simultaneously to a polynomial of the order three (for details, see text).

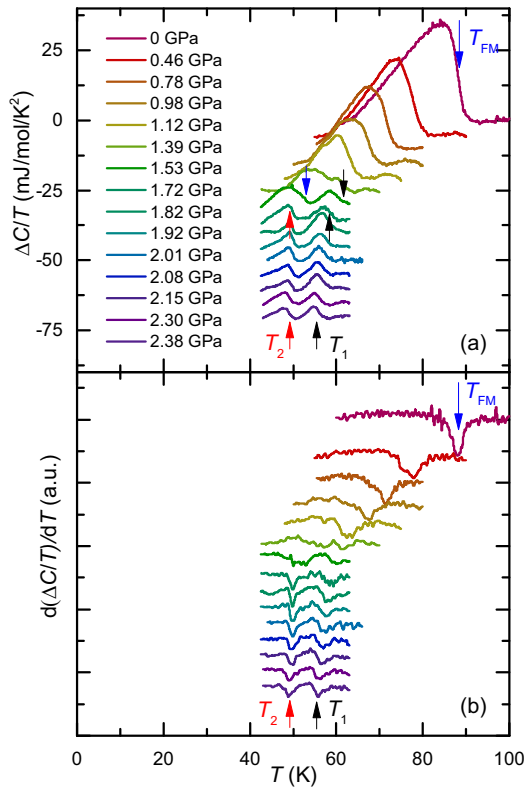


FIG. 10. Anomalous contribution to the specific heat, $\Delta C/T$, (a) and temperature derivative of this data, $d(\Delta C/T)/dT$, (b) versus temperature, T , for LaCrGe_3 for finite pressures in the range $0 \text{ GPa} \leq p \leq 2.38 \text{ GPa}$. Blue, black, and red arrows in each panel exemplarily indicate the position of anomalies at T_{FM} , T_1 , and T_2 , respectively. In all panels, data were shifted vertically for clarity.

which should not be affected by the background subtraction procedure.

b. Position of anomalies in specific-heat data and criteria to determine transition temperatures

The so-obtained anomalous specific-heat contributions, $\Delta C/T$, as a function of temperature, T , are shown in Fig. 10(a), together with the temperature derivative of the same data in (b), for $0 \text{ GPa} \leq p \leq 2.38 \text{ GPa}$. The second-order FM transition at T_{FM} (indicated by the blue arrow) manifests itself in an almost mean-field-like jump in the specific heat, the size of which becomes progressively reduced with increasing pressure (note that a discussion of the specific heat signature of the first-order FM transition for $p \geq 1.53 \text{ GPa}$ will be given below). At $p = 1.39 \text{ GPa}$, a second, more subtle anomaly occurs on the high-temperature side of the FM specific-heat anomaly for the first time. This result suggests the appearance of a new phase transition, which was denoted by T_1 in the main text. Upon increasing the pressure slightly to 1.53 GPa , these two specific-heat anomalies at T_{FM} and T_1 , respectively, become more separated in temperature and thus clearly distinguishable. For even higher pressures, the anomaly, which we associate with T_{FM} , continues to drop (see below) but we also observe two specific-heat anomalies, which are separated by only $\approx 10 \text{ K}$ in temperature and almost

similar in size. The positions of both these anomalies are almost unchanged in temperature upon increasing pressure (compared to the strong suppression of the T_{FM} line with pressure). We thus assign the lower-temperature specific-heat anomaly for $p \geq 1.72 \text{ GPa}$ to another phase transition at T_2 , which is distinct from the FM transition. Note that the T_2 line has previously been reported in literature [32], based on electrical transport measurements, and was assigned to a new magnetic phase transition of likely modulated AFM_q . In the main text and also in the Appendix, we present neutron and further μSR data for high pressures, which strongly suggest a different interpretation of the magnetic state of the phase below T_2 .

To determine the transition temperatures T_{FM} , T_1 , and T_2 from the presented specific-heat data, the position of the minimum in $d(\Delta C/T)/dT$ was chosen [see position of the arrows, which are exemplarily shown for $p = 0 \text{ GPa}$ and 2.38 GPa in Fig. 10(b)]. The application of this criterion yields transition temperatures that are very close to that obtained by iso-entropic construction.

c. Signature of ferromagnetic transition in specific-heat measurements at and beyond 1.53 GPa

In the discussion above as well as in the main text, we do not show any specific-heat signatures of the FM transition for $p \geq 1.53 \text{ GPa}$. The main reason for this is that we were not able to resolve a clear and sharp feature in the specific heat for these pressures (in contrast to the clear, huge, and sharp features in the thermal expansion coefficient, shown in the main text and below). We believe that this is due to a sizable amount of entropy being released upon cooling through T_1 and T_2 , which likely results in only a small amount of entropy being released on the subsequent cooling through T_{FM} . In turn, then we expect that the specific-heat feature becomes very small, likely below the limit below which we can separate it from the background. In addition, the transition changes its character close to 1.5 GPa (see discussion below) and the absolute value of dT_{FM}/dp gets larger upon increasing p . It is therefore reasonable to expect that any specific-heat feature above 1.5 GPa might be different in shape and broadened in temperature, making it hard to separate the feature from the (unknown) background contribution. Nonetheless, even if no clear feature can be observed in C/T (or $\Delta C/T$), a potential feature might show up more clearly in the temperature derivative of these data. For this reason, we show in Fig. 11(a) the temperature derivative of $\Delta C/T$ data across a wider temperature range. For this plot, $\Delta C/T$ was obtained by $\Delta C/T = (C(T, p) - C(T, p = 0.98 \text{ GPa}))/T$, with $C(T, p)$ being the temperature-dependent specific-heat data at the pressure of interest and $C(T, p = 0.98 \text{ GPa})$ the temperature-dependent specific-heat data at 0.98 GPa . This analysis is needed, since a simple polynomial fit (with order three) is not sufficient to describe the background over a very wide temperature range. In our approach, we assume that $C(T, p = 0.98 \text{ GPa})$, for which only a FM transition for high temperatures $T > 60 \text{ K}$ occurs, can be used as a good proxy for the background contribution for $T \lesssim 50 \text{ K}$, where we expect the FM transition to occur for $p \geq 1.53 \text{ GPa}$. The justification for this ansatz is based on

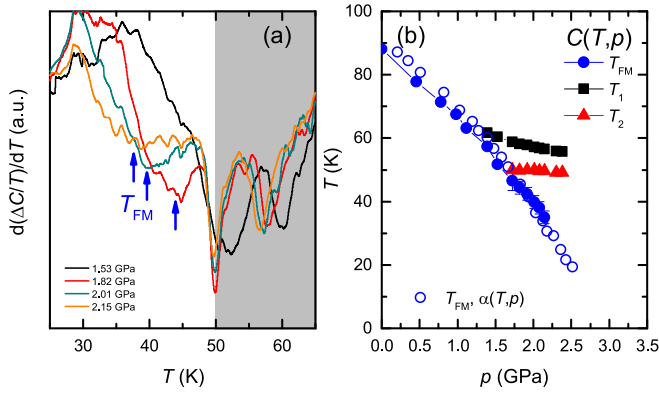


FIG. 11. (a) Derivative of the anomalous specific-heat contribution, $d(\Delta C/T)/dT$, versus T for LaCrGe_3 for selected pressures $1.53 \text{ GPa} \leq p \leq 2.15 \text{ GPa}$. ($\Delta C/T$) was obtained by subtracting the specific-heat data set at 0.98 GPa , which serves as a proxy for the background contribution for $T \gtrsim 50 \text{ K}$ from the measured data. The two large peaks for $T \gtrsim 50 \text{ K}$ (grey area) were identified as the anomalies at T_1 and T_2 in the main text. In addition, tiny and very broad anomalies, the positions of which are indicated by the arrows, can be identified at lower temperatures and are likely associated with the first-order ferromagnetic transition at T_{FM} for $p \gtrsim 1.5 \text{ GPa}$. (b) Temperature-phase diagram of LaCrGe_3 as constructed from specific-heat measurements under pressure. Blue solid circles, black solid squares, and red solid triangles correspond to T_{FM} , T_1 , and T_2 , respectively. Open blue symbols indicate the position of the clear anomalies at T_{FM} in the thermal expansion coefficient data (shown below).

the comparison of specific-heat data on LaCrGe_3 and the non-magnetic analog LaVGe_3 [35], which showed that the specific heat at temperatures well below the FM transition is dominated by nonmagnetic contributions. Indeed, as a result of our analysis, very subtle and progressively broader minima can be observed in the so-obtained $d(\Delta C/T)/dT$ data, the position of which (see arrows) coincide well [see Fig. 11(b)] with the positions of the sharp and clear anomalies in the thermal expansion coefficient (see main text and Fig. 13). Thus, we assume that this broad feature in the specific heat is indeed related to the FM ordering, in accordance with our hypothesis of smaller entropy associated with the ordering (compared to ambient pressure) and/or additional broadening of the feature. Nonetheless, from the specific-heat data alone, it would not be possible to infer the T_{FM} line for $p \geq 1.53 \text{ GPa}$ reliably.

3. Lattice parameters under pressure

a. Definition of physical quantities

Since we discuss and compare measurements from various techniques, which all give insight into the change of the crystalline lattice with pressure and temperature, we first want to define some of the measurement quantities here and elaborate which of the different experimental techniques yields insight into which quantity.

The temperature-dependent relative length change (or, alternatively, thermal expansion) of a macroscopic crystal along a crystallographic axis i , $(\Delta L/L)_i$ (with $i = ab, c$ for a hexag-

onal system, such as LaCrGe_3) is defined as

$$\begin{aligned} (\Delta L/L)_i(T, p = \text{const}) \\ = \frac{L_i(T, p = \text{const}) - L_i(T_{\text{ref}}, p = \text{const.})}{L_i(T_{\text{ref}}, p = \text{const})}, \end{aligned} \quad (\text{A1})$$

with $L_i(T, p = \text{const})$ being the absolute length of a crystal in the i direction at any given temperature, T , and T_{ref} being any reference temperature. The thermal expansion coefficient along a crystallographic axis i , α_i , is then defined as

$$\alpha_i = \frac{1}{L_i(T, p = \text{const})} \frac{\partial L_i(T, p = \text{const})}{\partial T}, \quad (\text{A2})$$

and is experimentally often determined to a very good approximation (since $\Delta L_i \ll L_i$) by

$$\alpha_i = \frac{1}{L_i(300 \text{ K}, p = \text{const})} \frac{d\Delta L_i(T, p = \text{const})}{dT}, \quad (\text{A3})$$

with $\Delta L_i = L_i(T, p = \text{const}) - L_i(T_{\text{ref}}, p = \text{const})$, and $L_i(300 \text{ K}, p = \text{const})$ being the length of the crystal at room temperature, which can be determined in an independent measurement. Note that due to the freedom in the choice of T_{ref} , ΔL_i can only be determined up to a constant. Since α_i , as defined above in Eq. (A3), is directly proportional to the temperature derivative of ΔL_i , the size of α_i is independent of the choice of T_{ref} . Note that in Eq. (A3), we set the normalization length in the denominator to $L_i(300 \text{ K}, p = \text{const})$, since $\Delta L_i \ll L_i$.

Experimentally, the relative length change, $(\Delta L/L)_i$, and the thermal expansion coefficient, α_i , can be determined from, e.g., capacitive dilatometry at ambient pressure or the strain-gauge technique for finite pressures. From neutron and x-ray diffraction measurements at ambient and finite pressures, the crystallographic lattice parameters $a = b$ and c (for a hexagonal crystal system, such as LaCrGe_3) can be inferred at any measured temperature and pressure. Each of these measurement quantities are related by simple equations, and we will do this explicit comparison for our data collection of LaCrGe_3 under pressure at the end of this section.

b. Functionality of the strain-gauge technique for the determination of the thermal expansion and the thermal expansion coefficient

Prior to the discussion of our various data sets, taken under finite pressures, we first want to demonstrate the functionality of our strain-gauge-based setup by comparing the relative length change, $(\Delta L/L)_i$, and the thermal expansion coefficient, α_i , obtained via the strain-gauge technique (at a relatively low applied pressure) to the data obtained by the technique of capacitive dilatometry at ambient pressure (see Fig. 12). Capacitive dilatometry is a well-established technique for the determination of the thermal expansion of solids and known for its extremely high sensitivity [65,66]. The capacitive dilatometry data, presented in Fig. 12, were obtained by using a dilatometer, which was described earlier in Ref. [67], in a Quantum Design PPMS, which provided the low-temperature environment.

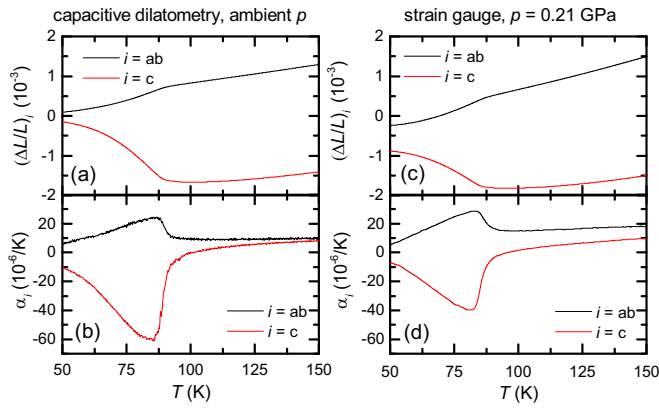


FIG. 12. Comparison of thermal expansion data on LaCrGe_3 , obtained by capacitive dilatometry (a), (b) and a strain-gauge-based method (c), (d). (a), (b) Relative length change, $(\Delta L/L)_i$ (a), and thermal expansion coefficient, α_i (b), versus temperature, T , along the crystallographic ab and c directions, obtained by utilizing a capacitive dilatometer at ambient pressure. (c), (d) Relative length change, $(\Delta L/L)_i$ (c), and thermal expansion coefficient, α_i (d), versus temperature, T , along the crystallographic ab and c directions, obtained by utilizing a strain-gauge-based method at $p = 0.21$ GPa inside the pressure cell. Due to the freedom of choice in T_{ref} , which causes that the relative length change can be only determined up to a constant, the $(\Delta L/L)_i$ values at 150 K were matched to the 150 K values from the capacitive dilatometry data.

Figures 12(a) and 12(b) show the temperature (T) dependence of $(\Delta L/L)_i$ and α_i for $i = ab, c$ at ambient pressure, as obtained from using the technique of capacitive dilatometry. (We use the notion of ab , since the a and b directions are equivalent in a hexagonal crystal system.) Upon cooling from 150 K, the crystal shrinks along both crystallographic inequivalent directions, as can be seen from a reduction of $(\Delta L/L)_i$, corresponding to positive values of α_i (with small directional anisotropy). Below 90 K, an anomalous behavior of $(\Delta L/L)_i$ and α_i can be observed, which is a result of the well-known FM ordering at $T_{\text{FM}} \simeq 89$ K [35]. In more detail, upon cooling through this FM transition, the length along the ab axes shrinks rapidly, whereas the length along the c axis shows a very pronounced increase. This response of the crystal lattice to the FM order is consistent with a picture of magnetoelastic effects resulting from dipolar coupling [68] of ferromagnetically aligned spins with moments aligned along the crystallographic c axis. The described relative length changes yield a positive anomaly in $\Delta\alpha_{ab}(T)$ and a negative anomaly in $\Delta\alpha_c(T)$, with $|\Delta\alpha_c(T)| \simeq 3|\Delta\alpha_{ab}(T)|$ ($\Delta\alpha_i(T)$) corresponding to the anomalous contribution to the thermal expansion coefficients after subtraction of nonmagnetic background contributions, not shown in Fig. 13. Given that the temperature dependence of $\alpha_i(T)$ is closely related to the temperature dependence of the specific heat, $C(T)$, via the (uniaxial) Grüneisen parameter, it can be expected that the anomalous contributions, $\Delta\alpha_i(T)$, are similar in shape to anomalous contributions to the specific heat, $\Delta C(T)$. Indeed, similar to the specific-heat measurements, the thermal expansion coefficients, $\alpha_i(T)$, display almost mean-field-like changes at the phase transition temperature T_{FM} . For reasons of consistency with the specific-heat data and the chosen crite-

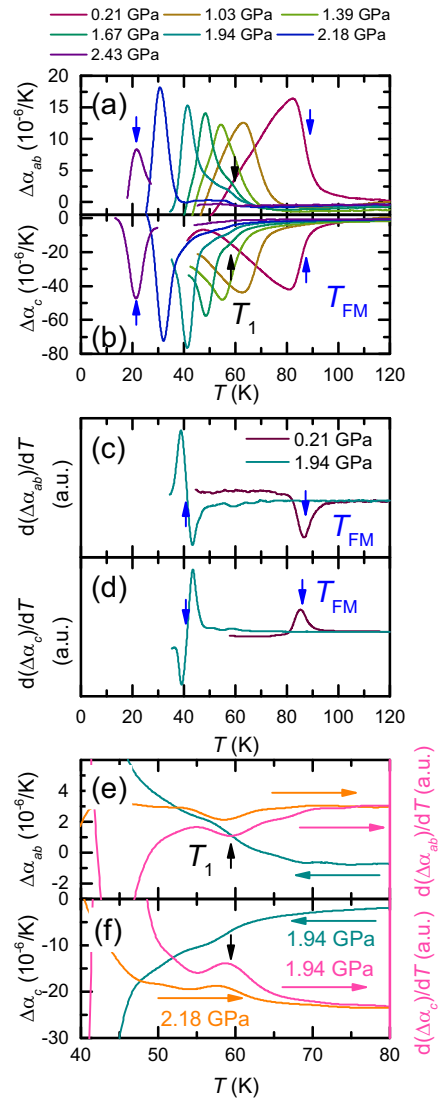


FIG. 13. Analysis of the thermal expansion anomalies. (a), (b) Anomalous contribution to the thermal expansion coefficient along the ab axes, $\Delta\alpha_{ab}$ (a), and along the c axis, $\Delta\alpha_c$ (b), versus temperature, T , of LaCrGe_3 for pressures $0.21 \text{ GPa} \leq p \leq 2.43 \text{ GPa}$. Blue (black) arrows indicate the criteria for the determination of T_{FM} (T_1). Note that the change in criterion for T_{FM} is related to the change of the character of the transition from second order to first order at $p_{\text{tr}} \simeq 1.5$ GPa (see text for details). Data between 30 K and 40 K are omitted due to an anomaly in the strain-gauge response that is not intrinsic to LaCrGe_3 . (c), (d) Derivative of the anomalous thermal expansion coefficients along the ab axes, $d(\Delta\alpha_{ab})/dT$, (c) and along the c axis, $d(\Delta\alpha_c)/dT$ (d) for $p = 0.21$ GPa and 1.94 GPa. The blue arrows indicate the criteria to determine T_{FM} from these data sets. (e), (f) Enlarged view on $\Delta\alpha_i$ (left axis) and $d(\Delta\alpha_i)/dT$ (right axis) for $i = ab$ (e) and $i = c$ (f) at $p = 1.94$ GPa around the phase transition temperature T_1 . The criterion, which was chosen to determine T_1 , is indicated by the black arrows. In each panel, $d(\Delta\alpha_i)/dT$ at $p = 2.18$ GPa is included to demonstrate that, if present, any feature at $T_2 \simeq 49$ K is distinctly smaller than the one at T_1 .

ria, the positions of the extrema in $d\alpha_i/dT$ (i.e., the minimum in $d\alpha_{ab}/dT$ and the maximum in $d\alpha_c/dT$) were chosen to determine $T_{\text{FM}} = 89.5$ K at ambient pressure.

For the comparison, Figs. 12(c) and 12(d) show the temperature dependence of $(\Delta L/L)_i$ and α_i for $i = ab, c$, obtained from the strain-gauge technique, as described in the section on experimental methods. The presented data were taken inside the pressure cell, which was closed hand-tight prior to the experiment without applying load to the piston. This procedure caused that the lowest-pressure measurements were actually already performed at a finite pressure of 0.21 GPa, as determined from the low-temperature Pb manometer. Whereas this small pressure leads to a small but measurable shift of the transition temperature, it does not compromise our comparison, since LaCrGe₃ still undergoes a FM transition with very similar responses of the crystalline lattice (as demonstrated by our x-ray and neutron-diffraction data under pressure, see below). Again, upon cooling from high temperature, we find a decrease of the length along both inequivalent directions (i.e., positive α_i values). Consistent with our dilatometry data, we find a strong decrease (large increase) of the length along the ab axes (c axis) at T_{FM} . The anomalies in $\alpha_i(T)$ with $i = ab, c$ are also almost mean-field-like. Applying the same criterion for the determination of T_{FM} as above yields $T_{\text{FM}}(0.21 \text{ GPa}) = 86 \text{ K}$ (see Fig. 13 for the temperature derivatives of these data).

This suppression of T_{FM} with modest pressures is fully consistent with our analysis of the phase diagram from specific-heat measurements. In terms of the absolute α_i [and $(\Delta L/L)_i$], we find that the maximum value of α_{ab} , determined from the strain-gauge technique, is similar to the one of the capacitive dilatometry data, whereas the value of α_c is smaller by about 1/3. Reasons for this discrepancy can be manifold. First, the strain gauges are rigidly glued to the samples. However, the glue will not transmit the strain perfectly, thus naturally leading to the observations of slightly smaller length changes in the strain-gauge measurements. If this was the case, then the fact that the α_{ab} values match better suggests that the strain transmission of the glue for the strain gauge of the ab axes was higher. Second, another option is related to the expansion of the tungsten-carbide samples, which we use for the subtraction of the intrinsic strain-gauge response. Strictly speaking, in our strain-gauge technique, we measure the length change of our sample relative to the one of the tungsten carbide pieces. However, tungsten carbide is known for its small expansivity [57] and thus this scenario is highly unlikely.

c. Anomalies in the thermal expansion coefficient under pressure and criteria for inferring phase transition temperatures

Figures 13(a) and 13(b) show the anomalous contributions to the thermal expansion coefficients, $\Delta\alpha_i$ with $i = ab, c$, of LaCrGe₃ for finite pressures up to 2.43 GPa. These $\Delta\alpha_i$ data were obtained by subtracting a background contribution, which was obtained by fitting a data set at 2.60 GPa, for which the FM transition T_{FM} is suppressed to $T < 10 \text{ K}$. We find that the above-described pronounced thermal expansion anomalies at T_{FM} , i.e., the positive anomaly in α_{ab} and the negative anomaly in α_c , are shifted to lower temperatures with increasing p . Importantly, in contrast to the signature of the FM transition in specific-heat measurements, the feature in the thermal expansion remains clear and measurable

over the full, investigated pressure range, thus allowing us to reliably determine the T_{FM} line across wide ranges of the phase diagram. At the same time, we find that the shape of the expansion anomalies along both directions changes its shape upon increasing pressure. Specifically, the almost mean-field-type $\Delta\alpha_i$, with $i = ab, c$, anomalies for low pressures change into symmetric and sharp peaks for higher pressures. These changes of the anomaly shape strongly suggest a change of the character of the phase transition from second order to first order upon increasing pressure, consistent with previous reports [32] as well as the generic avoidance of FM criticality in itinerant ferromagnets. The detailed determination of the associated tricritical point at $(p_{\text{tr}}, T_{\text{tr}})$ from an analysis of the asymmetry and the width of the thermal expansion coefficient feature will be discussed below. Here, we would only like to discuss the implications for the choice of criterion to determine T_{FM} from the present thermal expansion coefficient data. For low pressures, the mean-field-type anomaly gives rise to a pronounced minimum in $d(\Delta\alpha_{ab})/dT$ (maximum in $d(\Delta\alpha_c)/dT$, as exemplarily shown in Figs. 13(c) and 13(d) for $p = 0.21 \text{ GPa}$. We chose the positions of these extrema to determine T_{FM} for low pressures. In contrast, the sharp anomaly in the thermal expansion coefficient for high pressures gives rise to an anomaly in $d(\Delta\alpha_i)/dT$ ($i = ab, c$) with pronounced over- and undershoots on the low- and high-temperature sides, see, e.g., the $p = 1.94 \text{ GPa}$ data sets in Figs. 13(c) and 13(d). Correspondingly, we chose the midpoint in $d(\Delta\alpha_i)/dT$ between the maximum and minimum values of the anomaly to determine T_{FM} for high pressures (see blue arrows).

In addition to the FM anomaly, a closer look on the $\Delta\alpha_i(T)$ ($i = ab, c$) data reveal a smaller, but nonetheless clear anomaly at T_1 . To show this, we present in Figs. 13(e) and 13(f) the $\Delta\alpha_i(T)$ (left axis) as well as the $d(\Delta\alpha_i)/dT$ (right axis) for $p = 1.94 \text{ GPa}$ on enlarged scales around T_1 . The anomalies in $\Delta\alpha_i(T)$ can be seen with bare eyes but become very obvious in $d(\Delta\alpha_i)/dT$, where we observe a minimum in $d(\Delta\alpha_{ab})/dT$ and a maximum in $d(\Delta\alpha_c)/dT$. As already pointed out in the main text, this result implies that the lattice responds in the same way to the phase transition at T_1 as to the FM order, albeit smaller in size, i.e., the crystal shrinks in the ab plane and expands along the c axis upon cooling. The positions of the extrema in $d(\Delta\alpha_i)/dT$ were used to infer T_1 .

However, the phase transition at T_2 , which gives rise to a clear specific-heat feature, does not result in a pronounced feature close to 50 K in the thermal expansion coefficient. To demonstrate this, we also added the data sets of $\Delta\alpha_i(T)$ ($i = ab, c$) for $p = 2.18 \text{ GPa}$ in Figs. 13(e) and 13(f), since the FM transition is suppressed well below 50 K for this pressure. No clear feature is discernible in either the ab axes or the c axis data. Thus, we can conclude that the anomalous lattice effects are distinctly larger at T_1 than at T_2 , however, both are distinctly smaller than the one induced by long-range FM ordering.

d. Lattice parameters under pressure from x-ray and neutron diffraction

In Fig. 14, we show the temperature dependence of the crystallographic lattice parameters, a and c , determined from

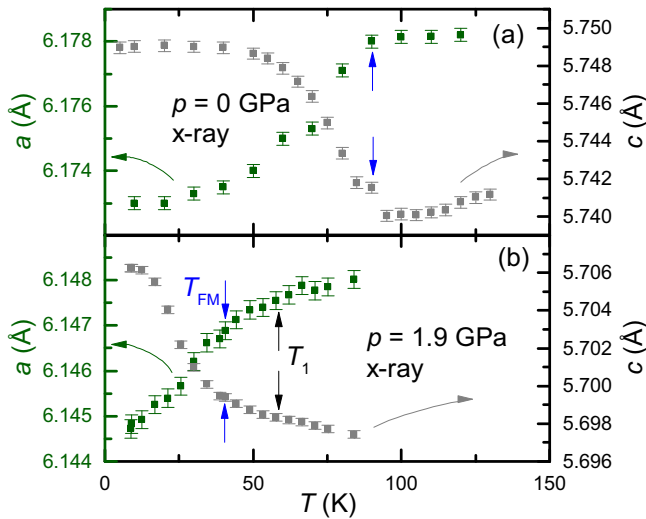


FIG. 14. Lattice parameters a (left axis) and c (right axis) at ambient pressure (a) and at $p = 1.9$ GPa (b), as determined from x-ray diffraction experiments. The positions of the arrows correspond to the transition temperatures determined from our thermodynamic measurements and approximately coincide with the points where the behavior of the lattice parameters deviates from the extrapolated high-temperature behavior.

x-ray diffraction measurements on single crystals at ambient pressure (a) and at $p = 1.9$ GPa (b). The c lattice parameters were determined by measuring the position of the (0 0 16) Bragg peaks with the Pixirad-1 detector at ambient pressure and the (0 0 4) Bragg peaks with the MAR345 detector while under applied pressure in the DAC. The a lattice parameters were determined the same way, using the position of the (16 0 0) and (2 2 0) Bragg peaks for ambient pressure and with applied pressure, respectively. At ambient pressure, the change of the lattice parameters is very consistent with the behavior found in measurements of the thermal expansion via capacitive dilatometry or the strain-gauge technique, which were discussed earlier in this section, i.e., the in-plane a lattice parameter shrinks and the c parameter increases upon cooling through the FM transition $T_{\text{FM}} \simeq 90$ K. The positions of the arrows correspond to the transition temperatures determined from our thermodynamic measurements and approximately coincide with the points where the behavior of the lattice parameters deviates from the extrapolated high-temperature behavior. The lattice parameters show a typical temperature dependence, consistent with the second-order nature of the phase transition. At 1.9 GPa, the FM transition is suppressed to much lower temperatures ($T_{\text{FM}} \simeq 40$ K) and still results in a strong increase of the c lattice parameter upon cooling, whereas the a lattice parameter shows a discernible decrease. In addition, a very subtle, kinklike feature might be discernible at much higher temperatures at $T \approx 60$ K at 1.9 GPa in the a and c lattice parameters, respectively (see black arrow). If indeed present, this feature coincides with T_1 . A clearer feature around T_1 on the basis of neutron-diffraction data will be presented below.

Figure 15 shows the temperature dependence of the a and c lattice parameters, inferred from the neutron-diffraction mea-

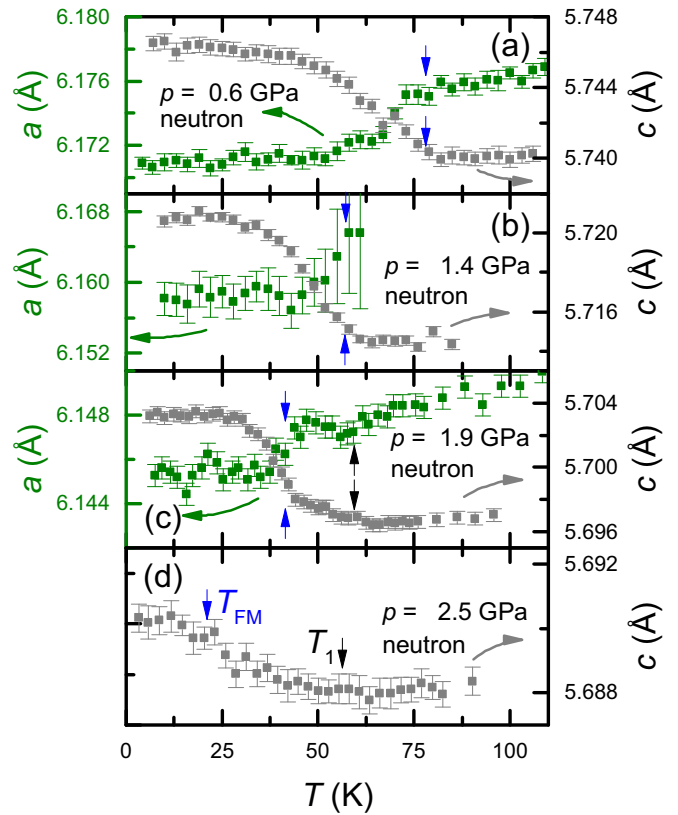


FIG. 15. Lattice parameters a (left axis) and c (right axis) at $p = 0.6$ GPa (a), at $p = 1.4$ GPa (b), at $p = 1.9$ GPa (c), and at $p = 2.5$ GPa (d), as determined from neutron-diffraction experiments [N1 (a)–(c), N2 (d)]. The positions of the arrows correspond to the transition temperatures determined from our thermodynamic measurements and approximately coincide with the points where the behavior of the lattice parameters deviates from the extrapolated high-temperature behavior.

surements on single crystals at HB1 for various pressures. Again, similar to the discussed other low-pressure data sets, the a (c) lattice parameters at $p = 0.6$ GPa show a decrease (an increase) upon cooling through $T_{\text{FM}}(p)$, which follow an order-parameter type of behavior, and thus, are consistent with the notion of a second-order phase transition. The c lattice parameter at 1.4 GPa also shows an order-parameter-type decrease at $T_{\text{FM}}(p)$. At 1.9 GPa, the FM transition is shifted to even lower temperatures in our neutron and x-ray diffraction data. In addition, the c lattice parameter shows a kink at much higher temperatures $T \approx 60$ K, which is thus likely associated with the phase transition at T_1 (this aspect becomes much clearer from a direct comparison of the lattice parameter data and the thermal expansion data, obtained by the strain-gauge data, which will be presented in the upcoming section). This kinklike feature in the c lattice parameter is accompanied by a very subtle change of the slope of the a lattice parameter. Increasing pressure even further to 2.5 GPa, we still find a kinklike feature in the c lattice parameter close to T_1 (as identified in our thermodynamic and transport data) and, upon further cooling, c shows an increase in the low-temperature region. This increase is likely associated with the (broadened) first-order FM transition as it gets suppressed closer to zero.

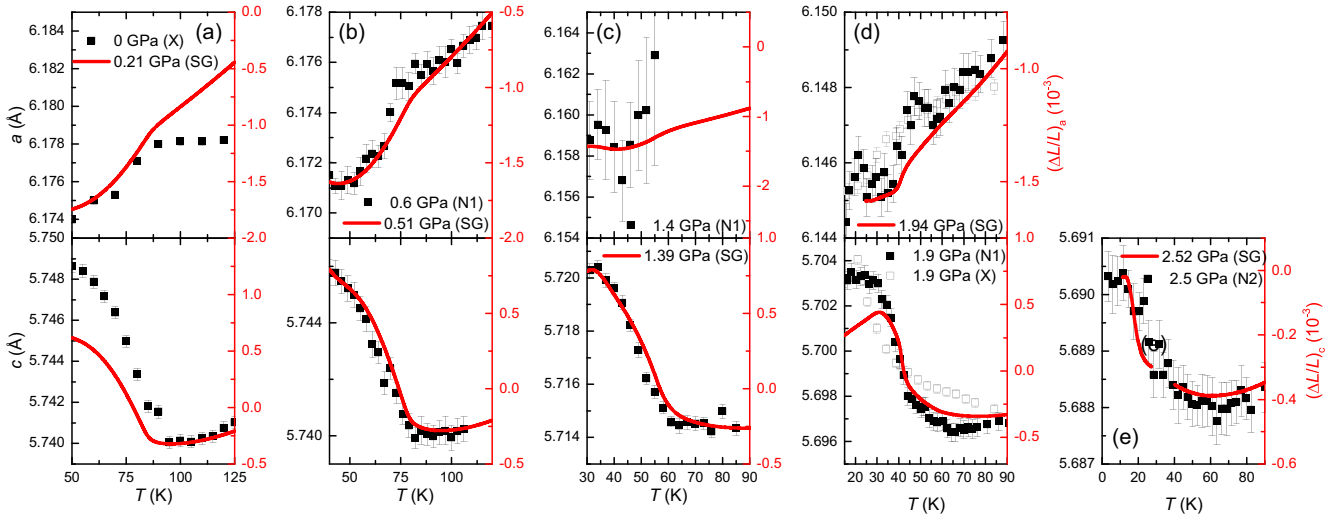


FIG. 16. Comparison of a and c lattice parameters of LaCrGe_3 , determined from x-ray and neutron-diffraction experiments, with the relative length change $(\Delta L/L)_a$ and $(\Delta L/L)_c$ of LaCrGe_3 , determined via the strain-gauge technique, as a function of temperature, T , for ambient and finite pressures. In each panel, the top shows the comparison of the a lattice parameter (left axis, symbols) with the relative length change $(\Delta L/L)_a$ (right axis, solid line), and the bottom shows the comparison of the c lattice parameter (left axis, symbols) with the relative length change $(\Delta L/L)_c$ (right axis, solid line). Note that for each panel the left and right axes are scaled such that they correspond to the same relative length changes. X-ray data (abbreviated as X) were taken at ambient pressure (a) and 1.9 GPa (d), neutron data (in cells N1 and N2) at pressures $p = 0.6$ GPa (b), 1.4 GPa (c), 1.9 GPa (d), and 2.5 GPa (e). Relative length change data (abbreviated as SG) were taken at $p = 0.21$ GPa (a), 0.51 GPa (b), 1.39 GPa (c), 1.94 GPa (d), and 2.52 GPa (e). The larger error bar in (c) of the lattice parameter data is related to shorter counting time.

Again, we will provide further evidence for the underlying phase transition in the next section, when we compare the different lattice parameter and length change data sets.

Comparison of lattice parameter data from x-ray and neutron-diffraction measurements under pressure to relative length change data, obtained from the strain-gauge-based technique under pressure. After the presentation of the measured data of relative length change and the lattice parameters under pressure, we want to turn to the explicit comparison of the various data sets, taken at very similar pressures. The result of this comparison is shown in Fig. 16. (Note that for each panel, the axes are scaled such that they correspond to the same relative length changes and thus the overlap of different data sets demonstrates the agreement of the data even on a quantitative level.) For the majority of the data sets, in particular, for all taken at finite pressures $p \geq 0.6$ GPa, we find good agreement of the lattice parameter data from neutron and x-ray diffraction experiments with the relative length change, determined from the strain-gauge technique. Only for the data at/close to ambient pressure, we find small discrepancies in the absolute values of the relative length change, as well as minor differences in the position of the FM anomaly. The latter can be assigned to the difference in pressure, at which the two data sets were taken. The reasons for the differences in absolute values only for this pressure are largely unknown and potential reasons were discussed in detail above when we compared the low-pressure strain gauge data to the data from capacitive dilatometry at ambient pressure.

Nonetheless, the good agreement of the diffraction and relative length change data provides strong support for statements made above. In particular, the broadened increase of the c lattice parameter at very low temperatures indeed coincides

with the increase of $(\Delta L/L)_c$ data, which can clearly be associated with a feature of the FM ordering. Thus, the c axis increase at low temperatures is also likely a result of the FM order, which is suppressed to very low temperatures.

4. Isostructural nature of all salient phase transitions

In this section, we show additional x-ray diffraction data, which demonstrate that all salient phase transitions, which were observed in our thermodynamic and diffraction data, only result in a change of the crystallographic lattice parameters but are not accompanied by any symmetry changes of the crystallographic structure. This allows us to exclude any type of charge-density wave or structural phase transition for the high-pressure phases in LaCrGe_3 .

a. High-energy x-ray diffraction of single crystals

High-energy x-ray diffraction data were taken on single crystals of LaCrGe_3 to search for any structural anomalies. These data are shown as two-dimensional images of the $(H H L)$ plane in Fig. 18 and as longitudinal cuts through the Bragg peak $(2 2 0)$ in Fig. 19 for $p = 1.5$ GPa, 1.9 GPa, and 4 GPa for several temperatures. We note that the previous study of LaCrGe_3 [32,33] suggested that at $p = 4$ GPa and base temperature, LaCrGe_3 is in the new magnetic phase (see Fig. 17). Therefore, we expect to probe the properties of the new phase at 4 GPa, well separated from the low- p ferromagnetism. From the data in Fig. 18, we see no indication of additional Bragg peaks from LaCrGe_3 within a dynamical range of 10^5 , which indicates that there is no superstructure and no charge-density wave at any pressure. In addition, we show in Fig. 19 that we did not observe splitting

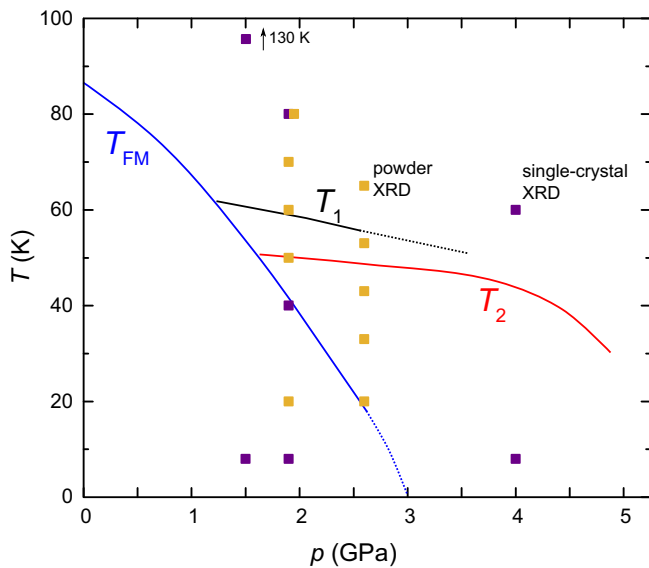


FIG. 17. Temperature-pressure phase diagram of LaCrGe_3 , as obtained from the present study, showing the phase transition lines at T_{FM} , T_1 , and T_2 . High-pressure data for T_1 is taken from previous works [32,33]. Purple (dark yellow) symbols indicate the temperature/pressure combinations for which single-crystal (powder) x-ray diffraction data were taken with high statistics and which are shown in Figs. 18–20. Dotted lines correspond to extrapolation and not actual data.

or broadening of the Bragg peaks which would indicate a symmetry-lowering lattice distortion.

At ambient pressure, LaCrGe_3 was reported to adopt a hexagonal perovskite structure with space group $P6_3/mmc$ [69,70]. The single-crystal x-ray data indicates that the crystal structure remains hexagonal or trigonal and with a c -glide plane parallel to the uniaxial c direction through all salient phase transitions at all pressures. Given these constraints and the parent space group of LaCrGe_3 , $P6_3/mmc$ [69,70], several structural phases can occur, (i) $P6_3/mmc$, (ii) $P\bar{6}2c$ with a rotation in the ab plane of the triangularly arranged Ge atoms as a new degree of freedom, (iib) $P6_3mc$ with a shift of the La planes in the c direction relative to the Cr and Ge planes, and (iii) $P31c$ which is a combination of both. Phase transitions from the parent space group, $P6_3/mmc$, to $P\bar{6}2c$, $P6_3mc$, or $P31c$ would leave the lattice symmetry and the reflection conditions unchanged but could be differentiated from analysis of the Bragg peak intensities. To investigate whether there is a change of Bragg peak intensities, we performed an x-ray diffraction study on powder samples under pressure, the results of which will be discussed in the following.

b. Powder x-ray diffraction in a DAC

To measure the largest number of Bragg peak intensities possible at once within a DAC, we recorded x-ray diffraction data on powder samples of LaCrGe_3 down to 20 K. To minimize the effect of the small sample size and create a better polycrystalline average, individual scans at each temperature were measured on a MAR345 with the DAC at different an-

gles along an axis perpendicular to the incident beam while rocking the sample along another axis perpendicular to the incident beam. Each scan was azimuthally integrated and combined at each temperature and pressure measured. To reduce the impact of comparatively large single-crystal grains in the sample, very strong individual Bragg peaks were excluded from the azimuthal integration. The powder x-ray diffraction data processed this way is shown in Fig. 20, and shows virtually no change in the Bragg peak intensity as a function of temperature. The single-crystal and powder x-ray diffraction data strongly indicate that all phase transitions for LaCrGe_3 are isostructural in nature.

5. Magnetism under pressure from neutron and μSR studies

a. Neutron scattering under pressure

In Fig. 21, we show the integrated intensity data as a function of temperature of the (1 0 0) Bragg peak (a) and the (0 0 2) Bragg peak (b), which were obtained in neutron-diffraction experiments at HB1. For the (1 0 0) Bragg peak, we find a clear increase of the intensity upon cooling through the FM transition temperature $T_{\text{FM}}(p)$ (see blue arrows). The positions of the arrows correspond to the transition temperatures determined from our thermodynamic measurements and approximately coincide with the points where the behavior in the integrated intensities deviates from the extrapolated high-temperature behavior. The increase of the (1 0 0) Bragg peak is fully consistent with a FM order with moments aligned along the crystallographic c axis [70] and corresponds to $1.5(3) \mu_{\text{B}}$ at $p = 0$ GPa and $T = 5$ K. The value of the magnetic moment was determined from the (1 0 0) Bragg peak intensity, I_{100} , relative to a set of nuclear Bragg peaks and compared to calculated intensities [71]. For low pressures, the temperature dependence of the (1 0 0) Bragg peak shows a typical order-parameter behavior and is thus fully consistent with the second-order nature of the FM transition. Upon increasing pressure, T_{FM} is shifted to lower temperatures. For 1.9 GPa, the ordered moment is $1.4(3) \mu_{\text{B}}$ at $T = 9$ K.

We also observe an increase of the (0 0 2) Bragg peak intensity for almost all pressures at T_{FM} , as shown in Fig. 21(b). This effect, however, is likely not related to the magnetic order itself, but rather due to extinction effects, i.e., a change of the mosaicity of the crystal upon cooling through a transition can lead to a sudden increase of the neutron intensity as a consequence of the suppression of multiple scattering [72]. For example, a magnetic transition can change the mosaicity of a crystal through magnetoelastic effects and the formation of magnetic domains. With x-ray single-crystal diffraction, we verified the presence of strong extinction effects by Renninger scans [73] of Bragg peaks by rotating the crystal about the axis of the scattering vector. We found a variation of Bragg peak intensities as the azimuthal angle is changed at ambient pressure, characteristic for strong extinction effects. Extinction effects can be expected to be large for strong nuclear Bragg peaks, such as the (0 0 2) Bragg peak, whereas they are negligible for weak nuclear Bragg peaks, such as (1 0 0). In addition, if the change in intensity of the (0 0 2) Bragg peak was magnetic in nature, then other Bragg peaks, e.g., (1 0 2) and (2 0 2), corresponding to the same magnetic order, should show a similar increase of magnetic intensity,

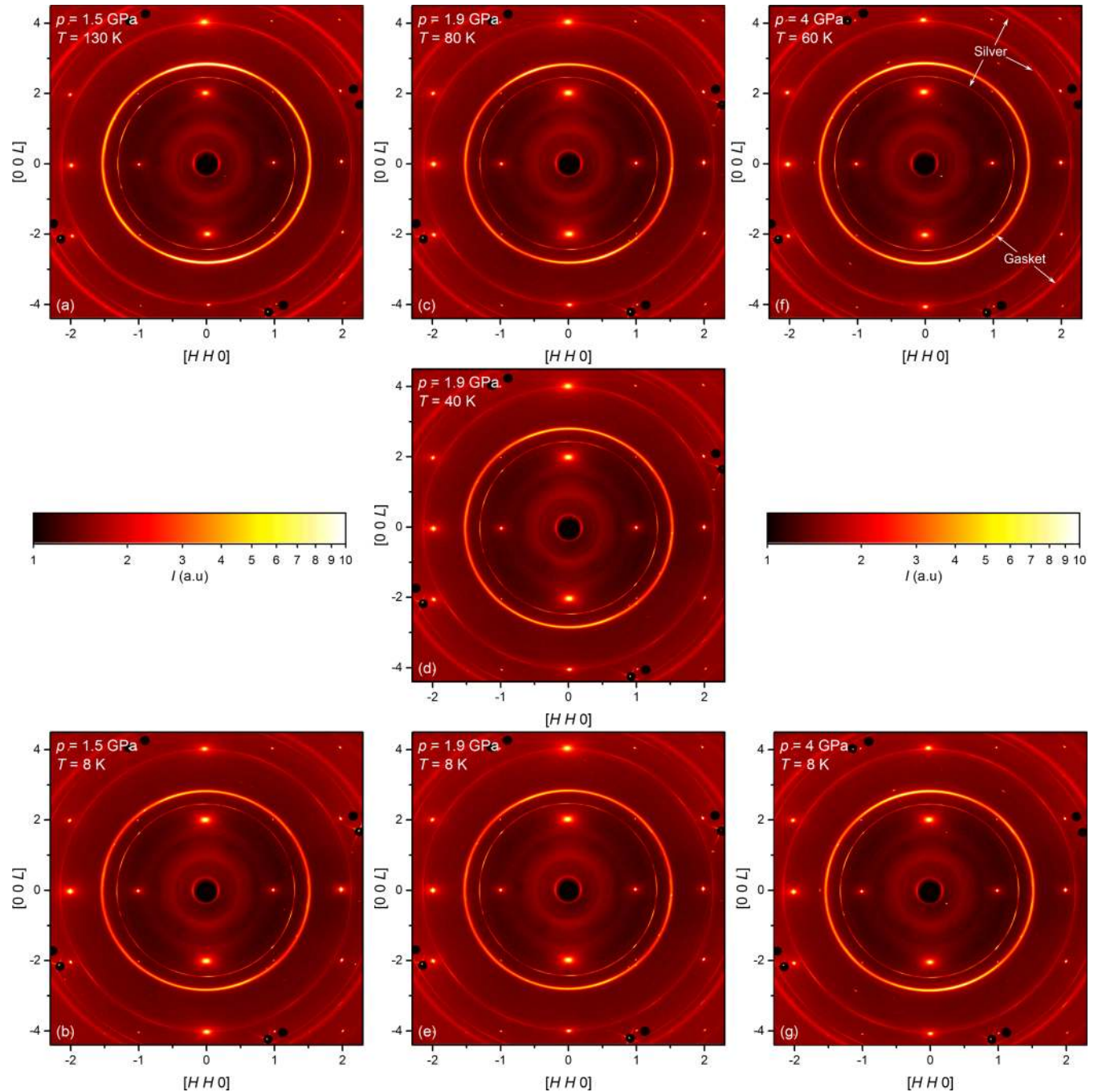


FIG. 18. High-energy x-ray diffraction data on a LaCrGe_3 single crystal measured at different temperatures and pressures. Image plots of the $(HH L)$ plane are shown in each panel with intensities color coded to a log plot as indicated in the color bars. The large, noncentral, black circles are from masking the Bragg peaks from the diamond anvils in the DAC, whereas the polycrystalline rings are from the silver foil and the stainless steel gasket, as exemplarily indicated by the white arrows in the top right panel.

which was not observed in our experiment. Since extinction effects are dependent on factors such as the size and shape of a specific sample, the strain applied to a specific sample and the scattering configuration, the effect is expected to be strongly sample dependent. For our measurements on LaCrGe_3 , extinction release coincides with T_{FM} for $p \leq 1.9$ GPa (see blue arrows). For higher pressures, the effects of extinction release are weaker. At 2.5 GPa, there is an increase of the $(0\ 0\ 2)$ intensity upon cooling but we cannot assign a characteristic

temperature solely on the neutron data, whereas for 3.5 GPa no increase can be observed.

Now we return to the survey of potential magnetic Bragg peaks for $p \gtrsim 1.9$ GPa, related to the new magnetic phases associated with T_1 and T_2 . In Figs. 22 and 23, we show scans along the high-symmetry H and L directions over wide regions of reciprocal space at base temperature for pressures of 1.9 GPa [(a)–(c)], 2.5 GPa [(d)–(f)], and 3.5 GPa [(g)–(i)]. Based on our T - p phase diagram, LaCrGe_3 is ordered

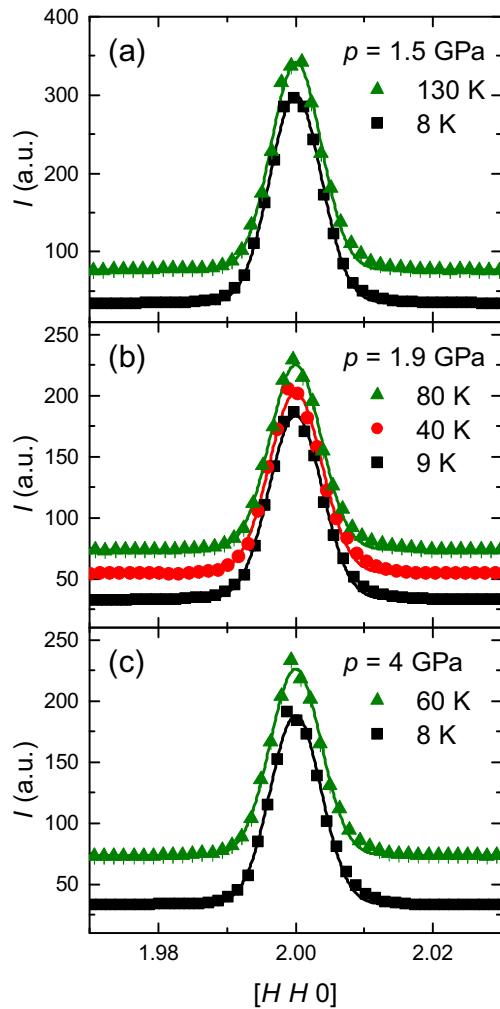


FIG. 19. Cuts along the $(H H 0)$ direction of the $(2 2 0)$ peak from high-energy x-ray diffraction data on a LaCrGe_3 single crystal under pressure. The data shows no peak splitting or broadening, indicating the absence of a symmetry-lowering structural phase transition. Cuts of the $(2 2 0)$ peak are shown at several temperatures for $p = 1.5$ GPa (a), 1.9 GPa (b), and 4 GPa (c). Data are offset for clarity.

ferromagnetically at base temperature for 1.9 GPa and 2.5 GPa and is in the new magnetic phase for 3.5 GPa, for which a modulated AFM_q was expected [32,33]. We do not observe a significant intensity of the $(1 0 0)$ Bragg peak for 2.5 GPa and 3.5 GPa. The nuclear contribution to the Bragg peak is likely reduced due to pressure-induced shifts of atomic positions and changes of lattice parameters. At the same time, the weak $(1 0 0)$ Bragg peak at 2.5 GPa implies at maximum only a weak FM contribution at base temperature [see inset in Fig. 22(d)]. This increase in the intensity is within the significance level of our experiment, but nonetheless consistent with the formation of FM order with small correlation length at base temperature (see also the large λ_T in μSR experiments at a similar pressure, discussed in the main text). At 3.5 GPa at low temperatures, a magnetic contribution to the $(1 0 0)$ Bragg peak can be ruled out within our experimental limits, discussed below. In addition, we do not observe magnetic superstructure peaks along the high symmetry di-

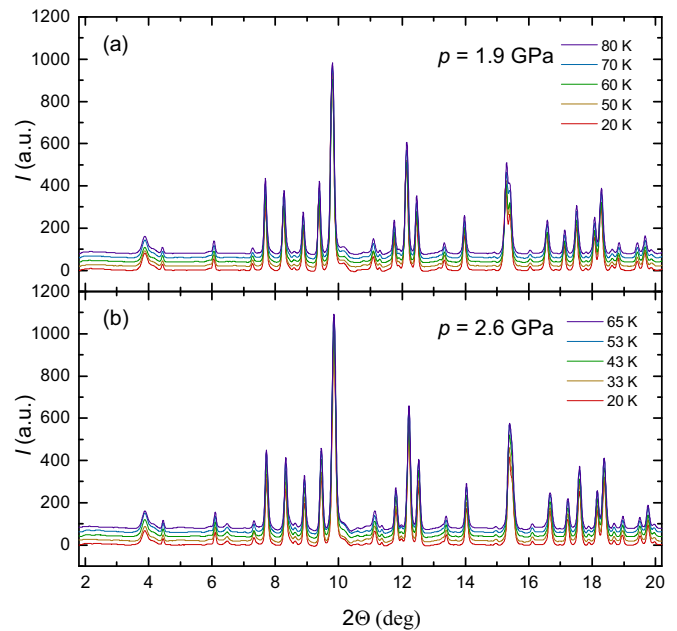


FIG. 20. Powder x-ray diffraction intensities of LaCrGe_3 under pressure. The data shows no significant change of peak intensities which would imply the absence of a symmetry-lowering structural component to all salient phase transitions at $p = 1.9$ GPa (a) and 2.6 GPa (b). Data are offset for clarity.

rections at any pressure, indicating the absence of AFM order, in particular for 3.5 GPa, for which LaCrGe_3 was proposed to be in the AFM_q region down to lowest temperature [32]. The only peaks observed during the experiment are structural Bragg peaks from LaCrGe_3 , the pressure cell, and the pressure medium, as indicated in Figs. 22 and 23.

Given the absence of magnetic Bragg peaks along the high-symmetry directions, we can calculate a lower boundary for the observable magnetic moment (μ) in our experiment for particular cases of long-range magnetic order. We discuss three cases of magnetic order which were suggested in Ref. [32]: (i) long-range FM with $\mu \parallel c$, (ii) an AFM structure consisting of FM- ab planes with $\mu \parallel c$, which are stacked along the c axis in a $+++++-----$ sequence, and (iii) the intermediate case with FM- ab planes stacked in a $100 \times +$ and $100 \times -$ sequence along the c axis. The FM order would yield a Bragg peak at $(1 0 0)$ with a minimum observable moment of $0.3 \mu_B$ at 3.5 GPa. The second structure would yield satellite peaks at positions $(1.1 0 0)$ and $(0.9 0 0)$, which are clearly separate from the $(1 0 0)$ Bragg peak. For those satellite peaks, we are sensitive to an ordered moment of $0.5 \mu_B$ at 3.5 GPa. We would observe the small- q peaks for the third structure as a broadened peak at position $(1 0 0)$, but the sensitivity for observing a peak at this position is the same as for the FM structure at 3.5 GPa, $\mu = 0.3 \mu_B$.

Since we found no evidence for AFM order along high-symmetry directions in the crystal, we then surveyed larger sections of reciprocal space using a CORELLI time-of-flight diffractometer. CORELLI allows for the simultaneous measurement of large sections of three-dimensional reciprocal space by utilizing a white-beam Laue technique with energy

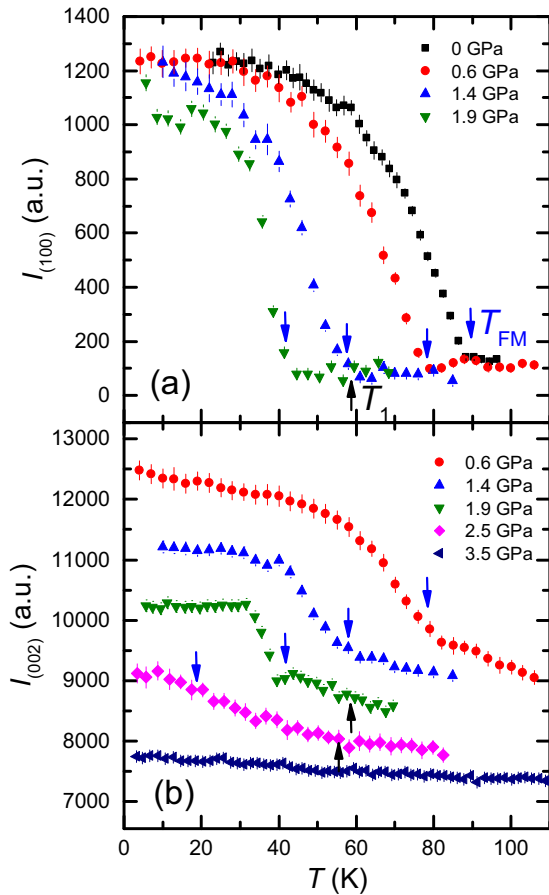


FIG. 21. Integrated intensity of the (1 0 0) Bragg peak (a) and the (0 0 2) Bragg peak (b) in elastic neutron-scattering experiments at HB1 on a single crystal of LaCrGe₃ under pressures up to 1.9 GPa (a) and 3.5 GPa (b). Blue arrows indicate the position of the ferromagnetic transition at T_{FM} . Data in (b) was offset for clarity. Data at ambient pressure were taken in experiment N0, data up to 1.9 GPa were taken in N1, data at 2.5 GPa and 3.5 GPa in N2. The positions of the arrows correspond to the transition temperatures determined from our thermodynamic measurements and approximately coincide with the points where the behavior in the integrated intensities deviates from the extrapolated high-temperature behavior.

discrimination by modulating the incident beam with a statistical chopper [58]. This allows CORELLI to efficiently separate the elastic and diffuse scattering from the sample and is useful for identifying short- and long-range order. By applying pressure in a DAC at CORELLI, we were able to reach pressures from 0.8 GPa to 3.2 GPa at base temperature. In Fig. 24, we show a clear increase of intensity of the (1 0 0) Bragg peak when cooling through the FM transition temperature at 0.8 GPa. This observation shows that we are sensitive to the FM transition at CORELLI and that we can expect to detect AFM order or short-range FM order with a minimum estimated correlation length of 15 nm with a similar magnetic moment for higher pressures. Note that the estimate of correlation length for our CORELLI experiment is 15 nm versus 12 nm for the HB1 experiment. As shown in the main text, we found no evidence of superstructure peaks indicative of AFM from LaCrGe₃ after an exhaustive search of peaks

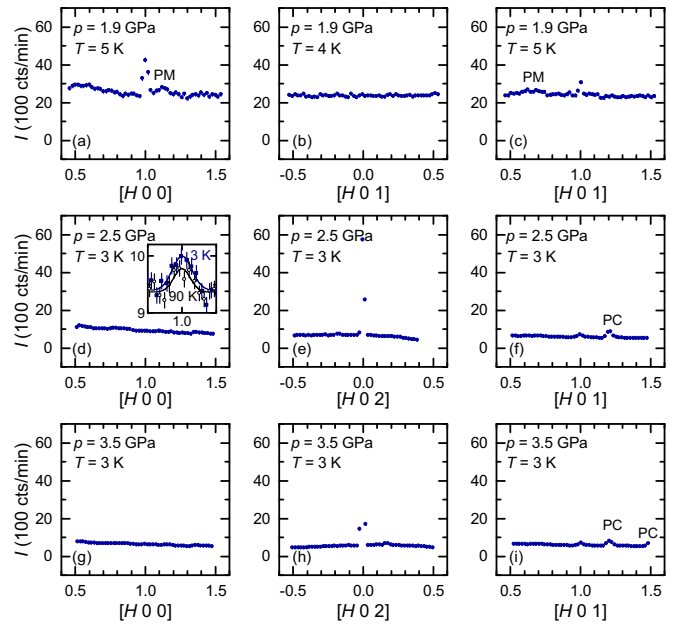


FIG. 22. Selected scans from neutron-diffraction experiments on a single crystal of LaCrGe₃ at HB1 along the high-symmetry directions [H 0 0] (a), (d), (g); [H 0 1] (b), (c), (f), (i); and [H 0 2] (e), (h) at base temperature for pressures of 1.9 GPa (a)–(c); 2.5 GPa (d)–(f); and 3.5 GPa (g)–(i). Different regions of reciprocal space were measured in the data due to the supports in the palm cubic cell blocking incoming and outgoing neutrons for some configurations. The labels Al, PC, and PM indicate that the observed peaks are associated with aluminum (Al), the pressure cell (PC), and the pressure medium (PM). Unlabeled peaks correspond to Bragg peaks associated with the crystal structure of LaCrGe₃. Data in (a)–(c) were taken in experiment N1, (d)–(i) in N2. Inset in (d) shows the [H 0 0] scan, measured with 5 min per data point, close to the (1 0 0) Bragg peak at 3 K and 90 K.

within the 3D reciprocal space at CORELLI. For the FM and AFM phases, introduced above in the discussion of the HB1 results, our sensitivity at CORELLI amounts to $\mu = 0.4 \mu_B$ for the FM phase with $\mu \parallel \mathbf{c}$ and $\mu = 0.7 \mu_B$ for the AFM (+++++-----) phase with $\mu \parallel \mathbf{c}$.

In conclusion, we found no indications of long-range magnetic order within the high-pressure phase in careful measurements along the high-symmetry directions on the triple-axis HB1, and within the full 3D reciprocal space measurements done at CORELLI. Summarizing all results from HB1 and CORELLI, our sensitivity for magnetic order would be a lower limit for correlation length of 15 nm for an ordered moment of $1.5 \mu_B$ like in the FM phase or a lower limit of $0.7 \mu_B$ for any long-range AFM order.

b. μ SR data under pressure

During a μ SR experiment, almost 100% spin-polarized muons are implanted into the sample of interest, where they thermalize at interstitial lattice sites. Once stopped, the muon precesses around the direction of the local magnetic field B at the stopping site with the Larmor frequency $\omega_m = \gamma_m \mu_0 B$ with $\gamma_m/(2\pi) = 135.5$ MHz/T being the muon gyromagnetic ratio. The muon is unstable with a lifetime of 2.2 μ s and

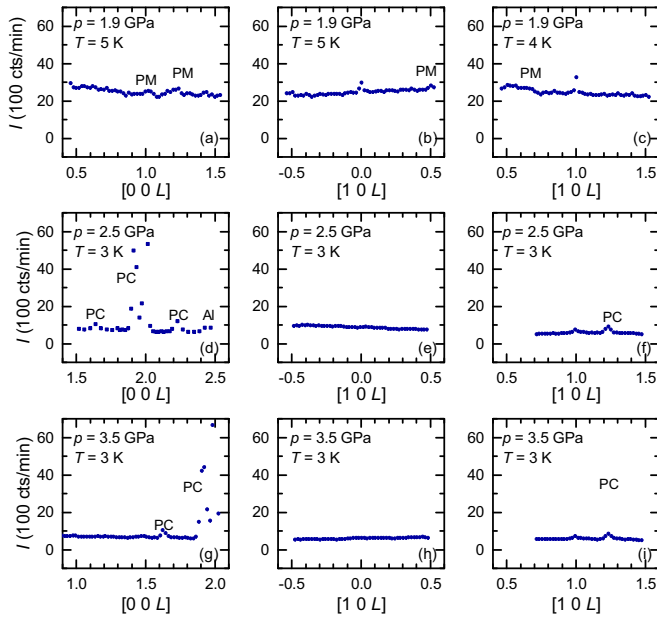


FIG. 23. Selected scans from neutron-diffraction experiments on a single crystal of LaCrGe_3 at HB1 along the high-symmetry directions $[0\ 0\ L]$ (a), (d), (g) and $[1\ 0\ L]$ (b), (c), (e), (f), (h), (i) at base temperature for pressures of 1.9 GPa (a)–(c), 2.5 GPa (d)–(f), and 3.5 GPa (g)–(i). Different regions of reciprocal space were measured in the data due to the supports in the palm cubic cell blocking incoming and outgoing neutrons for some configurations. The labels Al, PC, and PM indicate that the observed peaks are associated with aluminum (Al), the pressure cell (PC), and the pressure medium (PM). Unlabeled peaks correspond to Bragg peaks associated with the crystal structure of LaCrGe_3 . Data in (a)–(c) were taken in experiment N1, (d)–(i) in N2.

decays into a positron and two neutrinos. The time and direction dependence of the positron emission is monitored during a μSR experiment. From this information on the emitted positron, the muon precession and relaxation can be inferred and, thus, directly the local magnetic field in the sample. The muon therefore is a magnetic microprobe that allows for tracing of the internal magnetic fields at a local level and for investigations of the static and dynamic magnetism.

When μSR experiments are performed on a magnetic sample with simple magnetic order, which implies a well-defined magnetic field B at any of the n inequivalent muon stopping sites ($n \geq 1$, depending on the sample), then the superposition of the signals from all the muon stopping sites is observed experimentally. The measured asymmetry (i.e., the normalized difference between positron counts on the detectors in forward and backward directions) in zero magnetic field for a powder sample, or an aggregate of crystals with random orientation, is given by

$$A(0)P_{\text{ZF}}(t) = \sum_{i=1}^n A_i(0) \left[\frac{1}{3} \exp(-\lambda_{L,i}t) + \frac{2}{3} \exp(-\lambda_{T,i}t) \cos(\gamma_m B_{\text{int},i}t) \right], \quad (\text{A4})$$

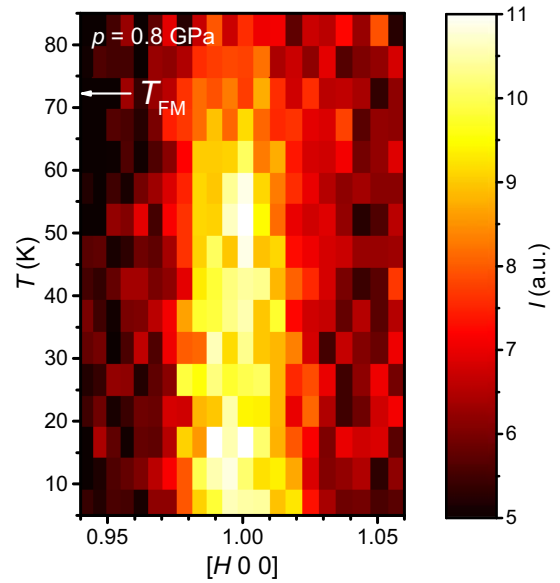


FIG. 24. Neutron-diffraction intensity of a LaCrGe_3 single crystal as a function of $[H\ 0\ 0]$ and temperature clearly showing the increase of $(1\ 0\ 0)$ peak intensity associated with the FM transition. Measurement was taken at CORELLI in a DAC with $p = 0.8$ GPa. The arrow, labeled T_{FM} , indicates the position of the ferromagnetic transition, as determined from our thermodynamic measurements under pressure. Data were taken in experiment N3.

with $A(0)$ ($A_i(0)$) the initial asymmetry of the muon ensemble (of the muon at the i th stopping site) and $P_{\text{ZF}}(t)$ the time-dependent polarization function of the muon ensemble. The spatial averaging due to the random orientation leads to a nonoscillating component with a weight of $1/3$ for muons, whose spins are parallel to the internal field vector at the stopping site, $B_{\text{int},i}$, and therefore show an exponential relaxation with rate $\lambda_{L,i}$, as well as an oscillating component with weight $2/3$, for which the muons precess around the internal field vector. The relaxation rate, $\lambda_{T,i}$, which is associated with the oscillating component, is a measure of the width of the static field distribution $\Delta B_{\text{int},i}/\gamma_m$, whereas $\lambda_{L,i}$ is solely related to dynamical magnetic fluctuations. Note that for LaCrGe_3 , an earlier, ambient-pressure study [32] showed that the muon time spectra was best fitted by considering three inequivalent muon stopping sites. However, the three internal field values $B_{\text{int},i}$ were found to be so close to each other that, for simplicity, we will consider only one muon stopping site for fitting the data inside the pressure cell, given that the higher background contribution in pressure-cell experiments does not allow for taking high-enough statistics to reliably distinguish different muon stopping sites with very similar internal fields.

In addition to ZF experiments, μSR measurements can also be performed in external fields. Here, wTF measurements, in which a small external field, $\mu_0 H_{\text{ext}}$, is applied perpendicular to the initial muon-spin direction, is a commonly used method to determine the onset magnetic transition temperature and the magnetic volume fraction. When muons stop in a non-magnetic sample, the external magnetic field causes a steady precession of the muon spin around its direction, giving rise to long-lived oscillations in the measured μSR asymmetry. In

contrast, when muons stop in a magnetically ordered sample, then the μ SR signal becomes more complex and reflects the precession around the vector combination of B_{int} and $\mu_0 H_{\text{ext}}$, which due to the random orientation of the crystallites leads to a broad distribution of precession frequencies. Therefore, the contribution to the muon asymmetry from muons, which do not experience a finite internal fields, can be accurately determined as a function of temperature. For the case of a wTF, i.e., $\mu_0 H_{\text{ext}} \ll B_{\text{int}}$, the fitting function of the μ SR asymmetry becomes simplified such that

$$A(0)P_{\text{wTF}}(t) = A_{\text{nmag}}(0) \cos(\gamma_m \mu_0 H_{\text{ext}} t + \phi) \exp\left(\frac{-\sigma_{\text{nm}}^2 t^2}{2}\right) + A_{\text{mag}}(0)P_{\text{ZF}}(t), \quad (\text{A5})$$

with $A_{\text{nmag}}(0)$ [$A_{\text{mag}}(0)$] the initial nonmagnetic [magnetic] asymmetry, ϕ a phase factor, σ_{nm} the relaxation rate caused by nuclear moments, and $P_{\text{ZF}}(t)$ the function defined in Eq. (A4).

Overall, in pressure-cell experiments, a large fraction of the muons stop in the pressure cell ($\approx 50\%$). This additional contribution has to be included in the data analysis, so the measured asymmetry $A(t)$ reads

$$A(t) = A_s(0)P_s(t) + A_{\text{pc}}(0)P_{\text{pc}}(t), \quad (\text{A6})$$

with $A_s(0)$ [$A_{\text{pc}}(0)$] being the initial sample [pressure-cell] asymmetry and $P_s(t)$ [$P_{\text{pc}}(t)$] the sample [pressure-cell] polarization function. The sample polarization function either corresponds to $P_{\text{ZF}}(t)$ for the case of ZF experiments, as defined in Eq. (A4), or to $P_{\text{wTF}}(t)$ for the case of wTF experiments [see Eq. (A5)].

The background of the pressure cell [47] is typically determined in an independent set of experiments and can then be described by two depolarization channels (one from nuclear moments and one from electronic moments), using a damped Kubo-Toyabe depolarization function,

$$A_{\text{pc}}^{\text{ZF}}(t) = A_{\text{pc}}^{\text{ZF}}(0) \left(\frac{1}{3} + \frac{2}{3}(1 - \sigma_{\text{pc}}^2 t^2) \exp(-\sigma_{\text{pc}}^2 t^2)\right) \times \exp(-\lambda_{\text{pc}} t), \quad (\text{A7})$$

with λ_{pc} the relaxation rate, which is related to electronic moments, and σ_{pc} the relaxation rate, related to the nuclear moments. For the case of LaCrGe_3 under pressure, it also needs to be taken into account that samples, which do exhibit a strong macroscopic magnetization, will induce a magnetic field in their surrounding, which can be felt by muons that stop in the pressure cell. Typically, this is the case for superconducting or ferro- and ferrimagnetic samples. As a result, the muons stopping regions of the pressure cell closest to the sample undergo a precession around the magnetic field, which is the vector sum of the applied field and the field induced by the sample with strong magnetization (the sum is denoted as B_{PC}). This leads to an additional depolarization of the muon spin polarization, the size of which depends on the external field, the field created by the sample as well as the stopping site distribution of the muons in the pressure cell with respect to the spatial distribution of B_{PC} . In these cases, the pressure cell contribution cannot be determined in an independent set of experiments or described by Eq. (A7) above, and instead follows in wTF experiments,

$$A_{\text{pc}}^{\text{wTF}}(t) = A(0) \exp(-\lambda_{\text{pc}} t) \exp(-\sigma_{\text{pc}}^2 t^2 / 2)$$

$$\times \cos(\gamma_m B_{\text{PC}} t + \phi), \quad (\text{A8})$$

with λ_{pc} the relaxation rate, the size of which is determined by the influence of a sample with macroscopic magnetization on the pressure cell as well as the electronic relaxation rate, and σ_{pc} the relaxation rate, related to the nuclear moments. The electronic relaxation rate is found to be temperature independent and was determined to be $\approx 0.05 \mu\text{s}^{-1}$ in the nonmagnetic state of LaCrGe_3 , i.e., for $T > T_{\text{FM}}$ at ambient pressure for the used pressure cell. Therefore, if the muons stopping in the pressure cell do not experience any field that is created by the sample, then $\lambda_{\text{pc}} \simeq 0.05 \mu\text{s}^{-1}$, and the pressure cell asymmetry shows long-lived oscillations. Instead, for $\lambda_{\text{pc}} \gtrsim 0.05 \mu\text{s}^{-1}$, the signal is damped, reflecting the additional depolarization of the precession of muons that stop in the pressure cell, as a result of the field created by the sample.

Following the same line of argument, any sample that exhibits a large, remanent magnetization will distort the pressure-cell μ SR signal. Thus, μ SR measurements inside the pressure cell also allow for the estimation of whether the sample exhibits a remanent magnetization or not. A remanent magnetization is typical for ferromagnets, however, the remanency can be very small, potentially even beyond the resolution of μ SR experiments.

Experimentally, the test for a remanent magnetization is performed in the following way. First, the sample is cooled below the transition temperature in ZF and an initial μ SR spectrum is recorded. In a next step, the external field is ramped isothermally to a specific, finite value, held constant for a short period of time, and then removed again. Then, at ZF, the μ SR spectrum is recorded again. The recorded pressure-cell response after the application and subsequent removal of the magnetic field can be described by the following function:

$$A(t) = A(0)[(1 - \zeta)G_{\text{KT}}(t) \exp(-\lambda_{\text{pc}} t) + \zeta], \quad (\text{A9})$$

with $1 - \zeta$ being the spectral weight of the relaxing component, $G_{\text{KT}}(t) = 1/3 + 2/3(1 - \sigma^2 t^2) \exp(-\sigma^2 t^2 / 2)$ being the Gaussian Kubo-Toyabe depolarization function reflecting the field distribution at the muon site created by nuclear moments, and λ_{pc} the exponential relaxation describing the influence of the sample on the pressure cell. Again, $\lambda_{\text{pc}} \simeq 0.05 \mu\text{s}^{-1}$ implies no remanent magnetization, whereas $\lambda_{\text{pc}} \gtrsim 0.05 \mu\text{s}^{-1}$ implies a remanent magnetization and the exact value of λ_{pc} is expected to be dependent on the external field that was applied prior to the collection of the spectrum (as long as the applied field is smaller than the saturation field). In the present experiment, we performed a set of these experiments at high pressures, $p = 2.55$ GPa, at three distinct temperatures. At each temperature, in total five different fields were applied and a spectrum was recorded each time after decreasing the respective field back to zero.

c. μ SR measurements in zero field at $p = 0.2$ GPa

Figure 25 shows selected ZF μ SR spectra of LaCrGe_3 at $p = 0.2$ GPa for temperatures in the range $10 \text{ K} \leq T \leq 89.5 \text{ K}$, i.e., across $T_{\text{FM}}(0.2 \text{ GPa}) \simeq 82 \text{ K}$. The $T = 10 \text{ K}$ data is shown again separately below in Fig. 28. For $T < T_{\text{FM}}$, a well-defined muon spin precession is observed, which confirms the presence of a finite internal field B_{int} . For

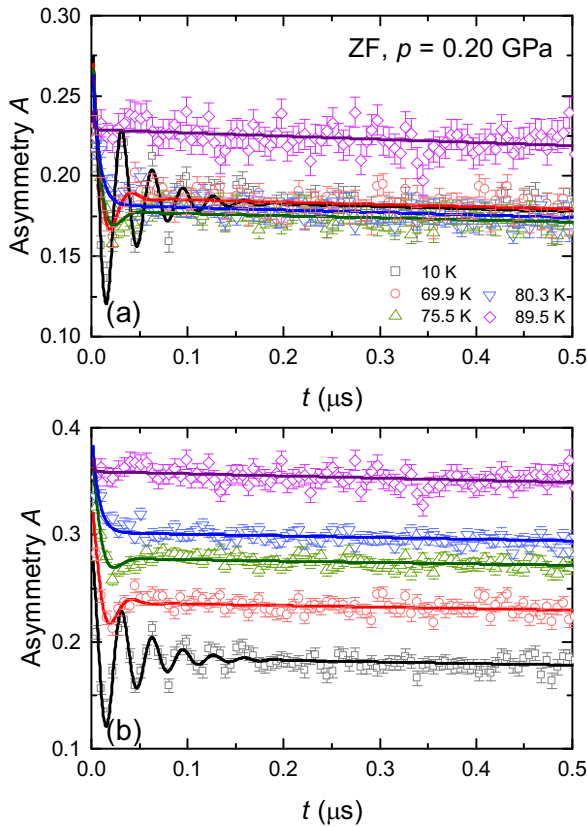


FIG. 25. Short-time μ SR spectra (symbols) of LaCrGe_3 , taken in zero field (ZF) and at pressure $p = 0.20$ GPa for different temperatures. Lines correspond to fits of the data to Eqs. (A4) and (A6). Data in (b) are the same as in (a) but offset for clarity.

temperatures just below T_{FM} , i.e., for $T = 80.3$ K, weak and highly damped oscillations are observed. For $T > T_{\text{FM}}$ (see $T = 89.5$ K data), no precession of the muon spins is discernible, indicating that $B_{\text{int}} = 0$. The solid lines in Fig. 25 correspond to fits to the experimental data to Eqs. (A4) and (A6). The temperature dependence of the fit parameters for all investigated temperatures will be discussed below.

d. μ SR measurements in weak-transverse field at $p = 0.2$ GPa

Next, we show selected μ SR time spectra of LaCrGe_3 at $p = 0.2$ GPa, which were taken in a wTF of 30 Oe after ZF cooling for various temperatures across T_{FM} in Fig. 26(a) as well as on enlarged scales around $t \approx 2.5 \mu\text{s}$ (b). For $T > T_{\text{FM}}$, large and only weakly damped oscillations with maximum amplitude close to 0.25, i.e., the maximum for the used spectrometer, are observed. This observation corresponds to the expected precession of the spins in the nonmagnetic sample and the nonmagnetic pressure cell induced by the wTF. In contrast, for $T < T_{\text{FM}}$, the oscillations are damped, since the sample exhibits a strong internal field, but also the pressure cell is exposed to a strong magnetic field, which is created by the FM sample inside the pressure cell. The ordering therefore leads to an additional depolarization of the muons, which explains the strongly reduced amplitude of the oscillations. The maximum size of the oscillation amplitude for $T < T_{\text{FM}}$ is fully consistent with full-volume fraction, which will be

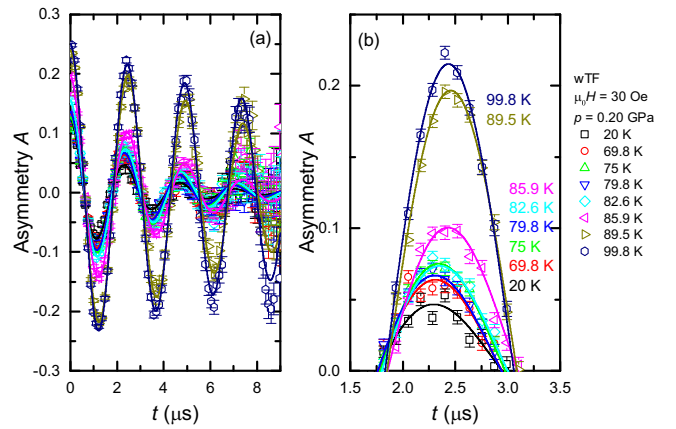


FIG. 26. Muon-time spectra (symbols) of LaCrGe_3 taken in a weak-transverse field (wTF) of 30 Oe and at a pressure $p = 0.20$ GPa for different temperatures (a), (b). (b) shows the data, presented in (a), on enlarged scales around the local maximum close to $t \approx 2.5 \mu\text{s}$. Lines correspond to fits of the data to Eqs. (A5) and (A6).

elucidated below in more detail when discussing the detailed evolution of the fit parameters with temperature, which are extracted from the fits to Eqs. (A5) and (A6) (solid lines in Fig. 26), and will be discussed in the following.

e. Temperature evolution of μ SR fitting parameters at $p = 0.2$ GPa and comparison with thermodynamic measurements

In Fig. 27, we show the temperature (T) evolution of the μ SR fitting parameters (a)–(d) at a pressure of 0.2 GPa. This includes the evolution of the internal field, B_{int} , (a) and the transverse relaxation rate, λ_{T} , (b) which were both extracted from fitting the ZF μ SR data, as well as the magnetic asymmetry, A_{mag} , (c) and the relaxation rate of the pressure cell, λ_{PC} , (d) which were extracted from fitting the wTF data. We compare this data with data of the specific heat, $\Delta C/T$, (e), the relative length change along the c axis, $(\Delta L/L)_c$ and the thermal expansion coefficient, α_c , (f) and the temperature derivative of the c -axis resistance, dR_c/dT , (g), all taken at similar pressure values.

We find that $B_{\text{int}} \simeq 2200$ Oe at lowest temperatures [see Fig. 27(a)], which is very similar to the previous μ SR data [32]. B_{int} decreases upon increasing T and extrapolates to zero close to $T_{\text{FM}} \approx 82$ K. At lowest temperatures, $\lambda_{\text{T}} \simeq 25 \mu\text{s}^{-1}$, somewhat larger but still consistent with previous reports [32], and increases with increasing temperature, until it reaches a peak at T_{FM} , above which λ_{T} decreases rapidly [see Fig. 27(b)]. This behavior of λ_{T} , which quantifies the width of the static field distribution at the muon stopping site, corresponds to the typical behavior for a sample which undergoes a magnetic transition. Only very close to the phase transition, the field distribution becomes wide as the field starts to occur in the sample when magnetic order develops, whereas well below the ordering temperature, λ_{T} is small, reflecting the well-ordered magnetism in LaCrGe_3 at 0.2 GPa (see below for a comparison of λ_{T} at 0.2 GPa and 2.55 GPa). A_{mag} is almost constant for $T \leq T_{\text{FM}}$ at a value of ≈ 0.12 [see Fig. 27(c)], which reflects that approximately 50% of

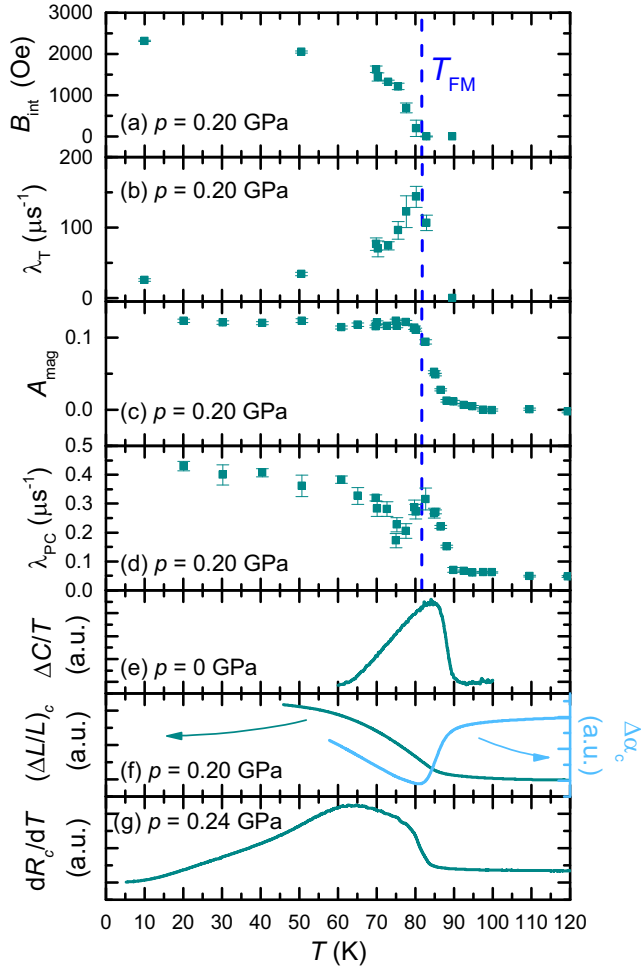


FIG. 27. Comparison of several low-pressure microscopic and thermodynamic data sets close to a pressure, p , of 0.2 GPa as a function of temperature, T . (a)–(d) Internal field, B_{int} (a), transverse relaxation rate λ_T (b), magnetic asymmetry, A_{mag} (c), and relaxation rate of the pressure cell, λ_{PC} , from zero-field (a), (b) and weak-transverse field (wTF) (c), (d) μSR measurements at $p = 0.2$ GPa. (e) Anomalous contribution to specific heat, $\Delta C/T$ at $p = 0$ GPa. (f) Relative length change and thermal expansion coefficient along the crystallographic c axis, $(\Delta L/L)_c$ (left axis) and α_c (right axis), respectively, at $p = 0.2$ GPa. (g) Temperature derivative of the resistance along the c axis, dR_c/dT , at $p = 0.24$ GPa. In (a)–(d), blue dashed lines indicate the position of the anomalies, associated with the ferromagnetic transition at T_{FM} .

the muons stop in the pressure cell. Therefore, this value of A_{mag} strongly suggests that the magnetic volume fraction reaches 100% at T_{FM} , given that the maximum asymmetry of the setup is close to 0.25, which was determined in a separate experiment. Above T_{FM} , A_{mag} decreases rapidly to zero, as the sample becomes nonmagnetic. $\lambda_{\text{PC}} \simeq 0.43 \mu\text{s}^{-1}$ at lowest temperatures [see Fig. 27(d)], the finite size of which reflects the influence of the magnetic field, created by the FM sample inside the pressure cell, on the pressure cell. Upon increasing T , λ_{PC} initially stays roughly constant and then starts to decrease as T is approaching T_{FM} . However, instead of λ_{PC} just approaching a value close to zero, the behavior of λ_{PC} is more complex. In more detail, λ_{PC} first goes

through a minimum at $T \approx 76$ K, followed by a maximum at ≈ 82 K and then decreases and saturates at a value close to zero for $T > T_{\text{FM}}$. This complex behavior of λ_{PC} was not discovered in the previous study [32], likely due to the large data point spacing in temperature. Whereas the maximum in λ_{PC} is highly likely related to the FM ordering at T_{FM} , we speculate that the minimum is rather related to the proposed crossover [33] from FM to FM2 in LaCrGe_3 upon cooling at low pressures. However, as we will show below and as was mentioned in the main text, we do not find any corresponding feature in our thermal expansion measurements. The observed features in the μSR fitting parameters at T_{FM} are consistent with the positions of the FM anomalies in the thermodynamic and transport studies of the present work (note that the shown specific-heat data set was taken at ambient pressure and thus at a slightly smaller pressure than the other data sets, which were taken at ≈ 0.2 GPa).

f. Direct comparison of low- and high-pressure μSR data

Finally, we want to explicitly compare the ZF muon-time spectra at low temperatures ($T = 10$ K) for 0.2 GPa [Fig. 28(a)] and 2.55 GPa [Fig. 28(b)], as well as the wTF time spectra at $T = 20$ K for the same pressures [Figs. 28(c) and 28(d)]. The comparison of the ZF spectra shows that the precession is much stronger damped for high pressures, as also quantified by the respective λ_T values, which are depicted in Fig. 27 and Fig. 4 in the main text, respectively. This implies that the static field distribution (i.e., the disorder in field the muon experiences) for 2.55 GPa is three to four times larger than the one at 0.2 GPa, whereas the size of the internal field B_{int} remains similar. Similar observations were also made in Ref. [32]. In addition, the comparison of the respective wTF data shows that the damping of the muon precession is larger for low pressures of 0.2 GPa than for high pressures of 2.55 GPa, i.e., that $\lambda_{\text{PC}}(0.2 \text{ GPa}) > \lambda_{\text{PC}}(2.55 \text{ GPa})$. This result implies that the macroscopic magnetization of the sample assembly is smaller for 2.55 GPa than for 0.2 GPa despite the very similar values of the internal field. Overall, in the main text, these observations have led us to a reinterpretation of the magnetism below T_2 for 2.55 GPa in terms of a short-range magnetically ordered state with FM component.

6. Estimation of the position of the tricritical point

In the following, we discuss our estimation of the position of the pressure-induced tricritical point at $(p_{\text{tr}}, T_{\text{tr}})$, at which the character of the FM transition changes from second order to first order. To this end, we will focus on an analysis of the anomalies in the thermal expansion coefficient, given the presence of pronounced features in this quantity over a wide range of the phase diagram.

a. Analysis of the shape of the anomaly

In thermodynamic quantities, a second-order phase transition often manifests itself in a strongly asymmetric, mean-field-type anomaly, whereas a first-order phase transition usually shows up as a symmetric, somewhat broadened peak. As discussed in the main text, we observe a change from an almost mean-field-type

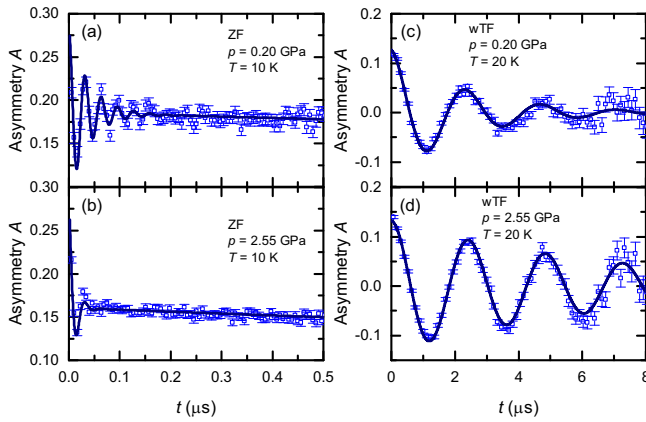


FIG. 28. Comparison of zero-field [ZF (a), (b)] and weak-transverse field [wTF (c), (d)] muon-time spectra (symbols) for low pressure, $p = 0.20$ GPa (a), (c) and high pressure, $p = 2.55$ GPa (b), (d). ZF data were taken at $T = 10$ K, wTF data were taken at $T = 20$ K. Lines are fits to the experimental data by Eq.(A4) for the ZF data and Eq. (A5) for the wTF data.

jump in the thermal expansion coefficient $\Delta\alpha_i$ for low pressures to an almost symmetric, sharp peak for high pressures. This signals a pressure-induced change of the character of the transition from second order to first order. To quantify this change and to determine the position of the associated tricritical point, we evaluated the asymmetry of the expansion anomaly $\Delta\alpha_a$ by using the following expression: $(T_r - T_m)/(T_m - T_l)$, with T_m being the temperature at which $\Delta\alpha_{ab}$ reaches its maximum value and T_r (T_l) being the higher (lower)

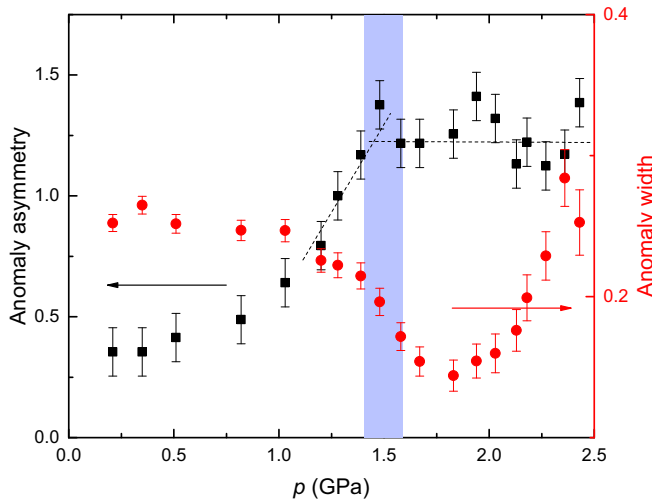


FIG. 29. Asymmetry (left axis) and width (right axis) of the thermal expansion anomalies in LaCrGe_3 along the crystallographic ab axis, which was shown in Fig. 13. The asymmetry was determined from $(T_r - T_m)/(T_m - T_l)$, with T_m being the temperatures at which the peak of the thermal expansion anomaly occurs and T_r and T_l being the temperatures at which the thermal expansion reaches 50% of the peak value, respectively. Correspondingly, the width was calculated as $(T_r - T_l)/T_m$. Dashed lines are guides to the eyes to highlight the change of behavior of the asymmetry close to 1.5 GPa.

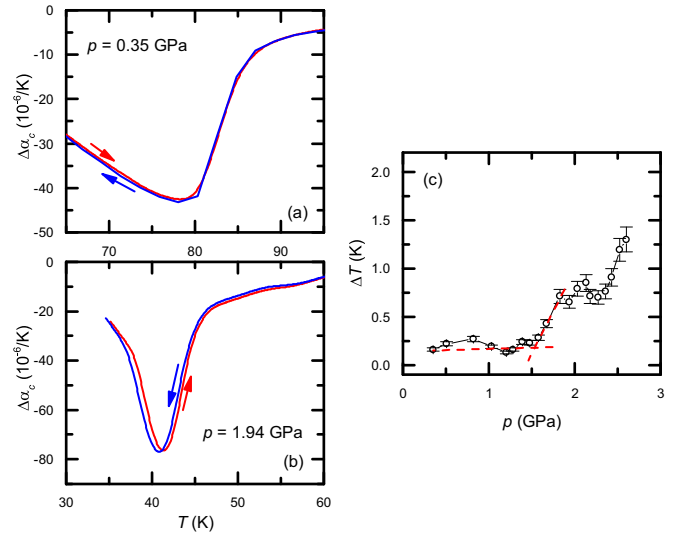


FIG. 30. Thermal hysteresis at the ferromagnetic transition in LaCrGe_3 . (a) Anomalous contribution to the thermal expansion coefficient along the c axis, $\Delta\alpha_c$, at $p = 0.35$ GPa upon warming (red) and cooling (blue). The rate of temperature change was ± 0.25 K/min; (a) $\Delta\alpha_c$ at $p = 1.94$ GPa upon warming (red) and cooling (blue); (c) thermal hysteresis, ΔT , defined as the difference between transition temperatures upon warming and cooling, as a function of pressure. Red dotted lines indicate the onset of a measurable thermal hysteresis beyond the experimental hysteresis of the setup.

temperature at which $\Delta\alpha_{ab}$ exhibits 50% of the maximum value of $\Delta\alpha_{ab}$. The evolution of the so-determined asymmetry is shown in Fig. 29 (left axis). For low pressures, the asymmetry parameter is less than 0.5, signaling a very asymmetric anomaly. With increasing pressure, the asymmetry parameter increases rapidly to a value close to 1 (corresponding to a perfectly symmetric peak) and flattens off (see dashed line) at a value of ≈ 1.2 . This behavior therefore meets the expectation for the above-described change from second order to first order. Thus, we use the pressure at which the asymmetry parameter levels off to determine the position of the tricritical point. This results in $p_{tr} = 1.5(1)$ GPa, and the corresponding $T_{cr} = 53(3)$ K was inferred from the thermodynamic phase diagram in Fig. 2 of the main text or Fig. 11(b). We can also consider the width of the $\Delta\alpha$ feature, which we determine via $(T_r - T_l)/T_m$ and is displayed on the right axis of Fig. 29. The width clearly shows a strong decrease right around p_{tr} , consistent with an increase in sharpness of the transition feature, once the transition becomes first order. We assign the subsequent increase of the width with pressure for higher pressures, which is on first glance not consistent with the notion of a sharp first-order transition, to an increased slope dT_{FM}/dp , which naturally accounts for an increase in broadening, the higher the pressure is.

b. Measurements of thermal hysteresis

As a complementary approach, we can also consider the evolution of the thermal hysteresis at the FM transition with pressure. In Figs. 30(a) and 30(b), we show two example data sets of the anomalous contribution to the thermal expansion

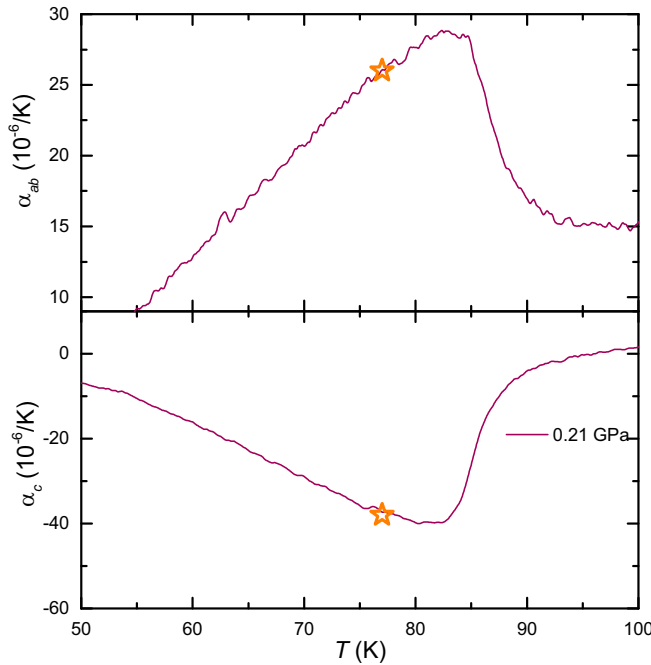


FIG. 31. Thermal expansion coefficients along the crystallographic ab direction, α_{ab} (top), and along the crystallographic c direction, α_c (bottom), versus T for LaCrGe₃ for $p = 0.21$ GPa. The orange stars indicate position of the minimum in λ_{PC} , inferred from the present μ SR measurements at a pressure of 0.2 GPa.

coefficient, $\Delta\alpha_c$, around the FM transition upon warming and cooling at $p = 0.35$ GPa (a) and 1.9 GPa (b). Whereas we find only a tiny thermal hysteresis for low pressure, which is probably related to the intrinsic hysteresis of our experimental setup, we observe a clear hysteresis for larger pressures. This clearly confirms that the transition becomes first order for higher pressures. A quantitative analysis of the evolution of the thermal hysteresis, ΔT , defined as the difference between transition temperatures upon warming and cooling, with pressure is shown in Fig. 30. ΔT starts to increase at ≈ 1.5 GPa, as visualized by the red lines, which is consistent with the position of the tricritical point, discussed above.

7. Probing the proposed FM2 transition

A previous study on LaCrGe₃ [33] suggested, based on resistance measurements at ambient and finite pressures $p \lesssim 1.8$ GPa and in zero and finite magnetic field, that LaCrGe₃ undergoes a crossover from the well-established FM state to another FM state, which was correspondingly labeled FM2. However, no clear feature associated with this crossover was detected in previous specific-heat measurements [35] at ambient pressure. In this section, we want to discuss to what extent our present set of thermodynamic, μ SR, and neutron-scattering measurements under pressure provide further insight into the presence of this crossover.

Figure 31 shows a plot of the thermal expansion anomalies α_i ($i = ab, c$) at $p = 0.21$ GPa. The orange stars indicate the position of minimum in λ_{PC} , which was observed in our μ SR data at 0.2 GPa (see Fig. 27) and which might be potentially related to the FM-FM2 crossover. However, our data of the

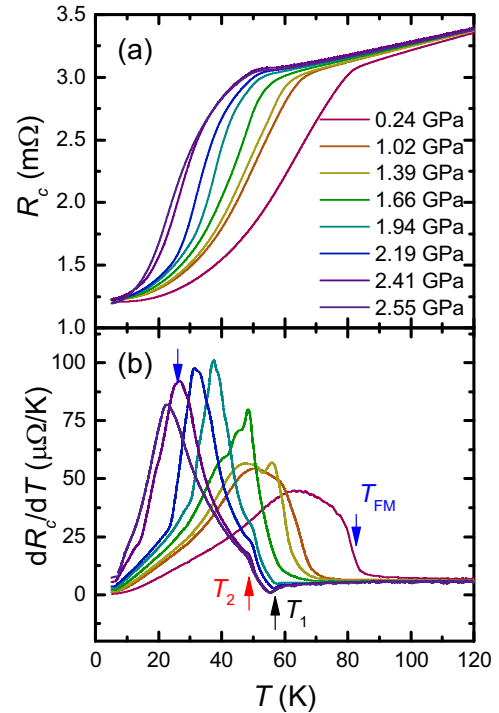


FIG. 32. (a) Resistance of LaCrGe₃ along the crystallographic c direction, R_c , as a function of temperature, T , for different pressures $0.24 \text{ GPa} \leq p \leq 2.55 \text{ GPa}$. (b) Temperature derivative of c axis resistance, dR_c/dT , versus T for the same pressures as in (a). Blue, black, and red arrows indicate the position of the anomalies that are associated with the phase transitions at T_{FM} , T_1 , and T_2 , respectively.

thermal expansion coefficients do not show any discernible feature at this temperature nor at any other temperature (also the ambient-pressure thermal expansion data does not reveal any signature of the crossover). Thus, we cannot provide any thermodynamic evidence for this crossover from our data. Similarly, we did not find any anomaly in our neutron data of the intensity of the (1 0 0) Bragg peak.

8. Resistance data under pressure

In this section, we want to provide more details of our resistance data set of LaCrGe₃ under pressure. We note that, in contrast to the previously published resistance under pressure data [32], which were performed with current in the ab plane (R_{ab}), we performed the present resistance data set with the current along the crystallographic c direction to infer R_c . In this way, we explore the directional anisotropy of the resistance to demonstrate that the herein-reported phase transition at T_1 leaves a clear fingerprint in $R_c(T)$ for high pressures.

Figure 32 shows selected data of R_c as a function of temperature, T , for different pressures in the range $0.24 \text{ GPa} \leq p \leq 2.41 \text{ GPa}$ [Fig. 32(a)], together with the temperature derivative of the same data in Fig. 32(b). For low pressures, we find a clear decrease of R_c upon cooling through the FM transition at T_{FM} , associated with the loss of spin-disorder scattering. For very high pressures, e.g., for 2.41 GPa, we find first a small increase of $R_c(T)$ upon cooling through T_1 before the resistance drops quickly below T_2 . This behavior

becomes more apparent when considering the T derivative of the R_c data. For low pressures, dR_c/dT shows a steplike feature at T_{FM} , which is followed by a broad maximum at lower temperatures. The broad maximum was also observed in previous work [33] and was associated with a crossover to another FM state at T_{FM2} . We have discussed the ambiguity of the thermodynamic evidence for this additional crossover in the previous section. Irrespective of this discussion, the midpoint of the steplike increase of dR_c/dT can be used to infer the transition temperature T_{FM} for low pressures. Upon increasing pressure, the steplike feature in dR_c/dT evolves into a clear peak. At the same time, above a finite pressure close to 1.5 GPa, the broad maximum associated with the potential T_{FM2} becomes indiscernible. Whenever dR_c/dT shows a clear peak rather than a steplike feature, see, e.g., the data sets for $p \geq 1.66$ GPa in Fig. 32(b), we used the peak position in dR_c/dT to infer T_{FM} . Note that we find a signature of the FM transition for $T \geq 5$ K in $R_c(T)$ up to 2.55 GPa, the highest pressure measured in this experiment (the corresponding data is shown in the main text). In addition to the features

that are associated with T_{FM} , we also find clear anomalies at T_1 and T_2 in dR_c/dT , see all data sets for $p \geq 1.94$ GPa in Fig. 32(b). The subtle increase in R_c at T_1 gives rise to a discernible minimum in dR_c/dT , the position of which we use to determine T_1 (see black squares). The transition at T_2 is associated with a decrease of $R_c(T)$ upon cooling, which gives rise to a clear kink in dR_c/dT . The position of this kink is used to infer T_2 and is visualized by the red triangles in Fig. 32(b). Altogether, this data set shows that the phase transition at T_1 leaves a clear fingerprint not only in $C(T)$ and $\alpha_i(T)$ but also in $R_c(T)$ as well.

We note that the critical pressure, at which the FM transition is fully suppressed, inferred from the herein presented resistance measurements with current along the c axis is larger than the one determined in Ref. [32], determined based on resistance measurements with current along the ab axis. The critical pressure inferred from our thermal expansion measurements is consistent with our c axis resistance measurements. The origin of the small discrepancy to the previous measurements is unclear at present.

-
- [1] P. C. Canfield and S. L. Bud'ko, *Rep. Prog. Phys.* **79**, 084506 (2016).
- [2] G. R. Stewart, *Rev. Mod. Phys.* **73**, 797 (2001).
- [3] C. Pfleiderer, S. R. Julian, and G. G. Lonzarich, *Nature* **414**, 427 (2001).
- [4] F. Lévy, I. Sheikin, and A. Huxley, *Nat. Phys.* **3**, 460 (2007).
- [5] Y. J. Uemura, T. Goko, I. M. Gat-Malureanu, J. P. Carlo, P. L. Russo, A. T. Savici, A. Aczel, G. J. MacDougall, J. A. Rodriguez, G. M. Luke *et al.*, *Nat. Phys.* **3**, 29 (2007).
- [6] N. T. Huy, A. Gasparini, D. E. de Nijs, Y. Huang, J. C. P. Klaasse, T. Gortenmulder, A. de Visser, A. Hamann, T. Görlach, and H. v. Löhneysen, *Phys. Rev. Lett.* **99**, 067006 (2007).
- [7] T. Westerkamp, M. Deppe, R. KÜchler, M. Brando, C. Geibel, P. Gegenwart, A. P. Pikul, and F. Steglich, *Phys. Rev. Lett.* **102**, 206404 (2009).
- [8] C. Pfleiderer, *Rev. Mod. Phys.* **81**, 1551 (2009).
- [9] S. Ubaid-Kassis, T. Vojta, and A. Schroeder, *Phys. Rev. Lett.* **104**, 066402 (2010).
- [10] S. S. Saxena, P. Agarwal, K. Ahilan, F. M. Grosche, R. K. W. Haselwimmer, M. J. Steiner, E. Pugh, I. R. Walker, S. R. Julian, P. Monthoux *et al.*, *Nature* **406**, 587 (2000).
- [11] D. Aoki, A. Huxley, E. Ressouche, D. Braithwaite, J. Flouquet, J.-P. Brison, E. Lhotel, and C. Paulsen, *Nature* **431**, 613 (2001).
- [12] J.-G. Cheng, K. Matsubayashi, W. Wu, J. P. Sun, F. K. Lin, J. L. Luo, and Y. Uwatoko, *Phys. Rev. Lett.* **114**, 117001 (2015).
- [13] S. Ran, C. Eckberg, Q.-P. Ding, Y. Furukawa, T. Metz, S. R. Sahaand, I.-L. Liu, M. Zic, H. Kim, J. Paglione *et al.*, *Science* **365**, 684 (2019).
- [14] P. Gegenwart, Q. Si, and F. Steglich, *Nat. Phys.* **4**, 186 (2008).
- [15] T. Shibauchi, A. Carrington, and Y. Matsuda, *Annu. Rev. Condens. Matter Phys.* **5**, 113 (2014).
- [16] M. Brando, D. Belitz, F. M. Grosche, and T. R. Kirkpatrick, *Rev. Mod. Phys.* **88**, 025006 (2016).
- [17] D. Belitz, T. R. Kirkpatrick, and T. Vojta, *Phys. Rev. B* **55**, 9452 (1997).
- [18] T. Vojta, D. Belitz, T. Kirkpatrick, and R. Narayanan, *Ann. Phys.* **8**, 593 (1999).
- [19] A. V. Chubukov, C. Pépin, and J. Rech, *Phys. Rev. Lett.* **92**, 147003 (2004).
- [20] D. Belitz, T. R. Kirkpatrick, and T. Vojta, *Rev. Mod. Phys.* **77**, 579 (2005).
- [21] G. J. Conduit, A. G. Green, and B. D. Simons, *Phys. Rev. Lett.* **103**, 207201 (2009).
- [22] D. Belitz and T. R. Kirkpatrick, *Phys. Rev. Lett.* **119**, 267202 (2017).
- [23] T. R. Kirkpatrick and D. Belitz, *Phys. Rev. Lett.* **124**, 147201 (2020).
- [24] M. Uhlarz, C. Pfleiderer, and S. M. Hayden, *Phys. Rev. Lett.* **93**, 256404 (2004).
- [25] C. Pfleiderer and A. D. Huxley, *Phys. Rev. Lett.* **89**, 147005 (2002).
- [26] P. G. Niklowitz, F. Beckers, G. G. Lonzarich, G. Knebel, B. Salce, J. Thomasson, N. Bernhoeft, D. Braithwaite, and J. Flouquet, *Phys. Rev. B* **72**, 024424 (2005).
- [27] A. Huxley, I. Sheikin, and D. Braithwaite, *Physica B* **284-288**, 1277 (2000).
- [28] E. Lengyel, M. E. Macovei, A. Jesche, C. Krellner, C. Geibel, and M. Nicklas, *Phys. Rev. B* **91**, 035130 (2015).
- [29] G. Abdul-Jabbar, D. A. Sokolov, C. D. O'Neill, C. Stock, D. Wermeille, F. Demmel, F. Krüger, A. G. Green, F. Lévy-Bertrand, B. Grenier *et al.*, *Nat. Phys.* **11**, 321–327 (2015).
- [30] S. Friedemann, W. J. Duncan, M. Hirschberger, T. W. Bauer, R. KÜchler, A. Neubauer, M. Brando, C. Pfleiderer, and F. M. Grosche, *Nat. Phys.* **14**, 62 (2018).
- [31] P. G. Niklowitz, M. Hirschberger, M. Lucas, P. Cermak, A. Schneidewind, E. Faulhaber, J.-M. Mignot, W. J. Duncan, A. Neubauer, C. Pfleiderer *et al.*, *Phys. Rev. Lett.* **123**, 247203 (2019).
- [32] V. Taufour, U. S. Kaluarachchi, R. Khasanov, M. C. Nguyen, Z. Guguchia, P. K. Biswas, P. Bonfà, R. De Renzi, X. Lin, S. K. Kim *et al.*, *Phys. Rev. Lett.* **117**, 037207 (2016).

- [33] U. S. Kaluarachchi, S. L. Bud'ko, P. C. Canfield, and V. Taufour, *Nat. Commun.* **8**, 546 (2017).
- [34] L. Xiang, E. Gati, S. L. Bud'ko, S. M. Saunders, and P. C. Canfield, [arXiv:2011.03086](https://arxiv.org/abs/2011.03086).
- [35] X. Lin, V. Taufour, S. L. Bud'ko, and P. C. Canfield, *Phys. Rev. B* **88**, 094405 (2013).
- [36] M. M. Wysokiński, *Sci. Rep.* **9**, 19461(2019).
- [37] V. Taufour, D. Aoki, G. Knebel, and J. Flouquet, *Phys. Rev. Lett.* **105**, 217201 (2010).
- [38] V. Taufour, U. S. Kaluarachchi, and V. G. Kogan, *Phys. Rev. B* **94**, 060410(R) (2016).
- [39] E. Gati, G. Drachuck, L. Xiang, L.-L. Wang, S. L. Bud'ko, and P. C. Canfield, *Rev. Sci. Instrum.* **90**, 023911 (2019).
- [40] E. Gati, L. Xiang, S. L. Bud'ko, and P. C. Canfield, *Ann. Phys.* **532**, 2000248 (2020).
- [41] N. Kabeya, K. Imura, K. Deguchi, and N. K. Sato, *J. Phys. Soc. Jpn.* **80**, SA098 (2011).
- [42] S. L. Bud'ko, A. N. Voronovskii, A. G. Gapotchenko, and E. S. Itskevich, *Zh. Eksp. Teor. Fiz.* **86**, 778 (1984).
- [43] <https://www.almax-easylab.com/ProductDetails.aspx?PID=50&IID=10029>.
- [44] N. Aso, Y. Uwatoko, T. Fujiwara, G. Motoyama, S. Ban, Y. Homma, Y. Shiokawa, K. Hirota, and N. K. Sato, *AIP Conf. Proc.* **850**, 705 (2006).
- [45] S. Dissanayake, M. Matsuda, K. Munakata, H. Kagi, J. Gouchi, and Y. Uwatoko, *J. Phys.: Condens. Matter* **31**, 384001 (2019).
- [46] B. Haberl, S. Dissanayake, F. Ye, L. L. Daemen, Y. Cheng, C. W. Li, A.-J. T. Ramirez-Cuesta, M. Matsuda, J. J. Molaison, and R. Boehler, *High Press. Res.* **37**, 495 (2017).
- [47] R. Khasanov, Z. Guguchia, A. Maisuradze, D. Andreica, M. Elender, A. Raselli, Z. Shermadini, T. Goko, F. Knecht, E. Morenzoni *et al.*, *High Press. Res.* **36**, 140 (2016).
- [48] A. Yaouanc and P. Dalmás De Réotier, *Muon Spin Rotation, Relaxation and Resonance* (Oxford University Press, Oxford, 2011).
- [49] U. Karahasanovic, F. Krüger, and A. G. Green, *Phys. Rev. B* **85**, 165111 (2012).
- [50] A. V. Chubukov and D. L. Maslov, *Phys. Rev. Lett.* **103**, 216401 (2009).
- [51] S. J. Thomson, F. Krüger, and A. G. Green, *Phys. Rev. B* **87**, 224203 (2013).
- [52] C. J. Pedder, F. Krüger, and A. G. Green, *Phys. Rev. B* **88**, 165109 (2013).
- [53] S. Lausberg, J. Spehling, A. Steppke, A. Jesche, H. Luetkens, A. Amato, C. Baines, C. Krellner, M. Brando, C. Geibel *et al.*, *Phys. Rev. Lett.* **109**, 216402 (2012).
- [54] M. S. Torikachvili, S. K. Kim, E. Colombier, S. L. Bud'ko, and P. C. Canfield, *Rev. Sci. Instrum.* **86**, 123904 (2015).
- [55] A. Eiling and J. S. Schilling, *J. Phys. F* **11**, 623 (1981).
- [56] L. Xiang, E. Gati, S. L. Bud'ko, R. A. Ribeiro, A. Ata, U. Tutsch, M. Lang, and P. C. Canfield, *Rev. Sci. Instrum.* **91**, 095103 (2020).
- [57] A. D. Krawitz, D. G. Reichel, and R. Hitterman, *J. Am. Ceram. Soc.* **72**, 515 (1989).
- [58] F. Ye, Y. Liu, R. Whitfield, R. Osborn, and S. Rosenkranz, *J. Appl. Crystallogr.* **51**, 315 (2018).
- [59] B. Haberl, S. Dissanayake, Y. Wu, D. A. Myles, A. M. dos Santos, M. Loguillo, G. M. Rucker, D. P. Armitage, M. Cochran, K. M. Andrews *et al.*, *Rev. Sci. Instrum.* **89**, 092902 (2018).
- [60] A. Drozd-Rzoska, S. J. Rzoska, M. Paluch, A. R. Imre, and C. M. Roland, *J. Chem. Phys.* **126**, 164504 (2007).
- [61] S. Klotz, K. Takemura, T. Strässle, and T. Hansen, *J. Phys.: Condens. Matter* **24**, 325103 (2012).
- [62] T. F. Smith and C. W. Chu, *Phys. Rev.* **159**, 353 (1967).
- [63] S. Klotz, J.-C. Chervin, P. Munsch, and G. L. Marchand, *J. Phys. D: Appl. Phys.* **42**, 075413 (2009).
- [64] N. Tateiwa and Y. Haga, *Rev. Sci. Instrum.* **80**, 123901 (2009).
- [65] T. Barron and G. White, *Heat Capacity and Thermal Expansion at Low Temperatures* (Springer Science+Business Media, New York, 1999).
- [66] R. KÜchler, T. Bauer, M. Brando, and F. Steglich, *Rev. Sci. Instrum.* **83**, 095102 (2012).
- [67] G. M. Schmiedeshoff, A. W. Lounsbury, D. J. Luna, S. J. Tracy, A. J. Schramm, S. W. Tozer, V. F. Correa, S. T. Hannahs, T. P. Murphy, E. C. Palm *et al.*, *Rev. Sci. Instrum.* **77**, 123907 (2006).
- [68] A. Lindbaum and M. Rotter, Spontaneous magnetoelastic effects in gadolinium compounds, in *Handbook of Magnetic Materials* (Elsevier, North Holland, 2002).
- [69] H. Bie, O. Y. Zelinska, A. V. Tkachuk, and A. Mar, *Chem. Mater.* **19**, 4613 (2007).
- [70] J. Cadogan, P. Lemoine, B. R. Slater, A. Mar, and M. Avdeev, in *Solid Compounds of Transition Elements II*, Solid State Phenomena, Vol. 194 (Trans Tech Publications Ltd., 2013), pp. 71–74.
- [71] J. Rodríguez-Carvajal, *Physica B: Condensed Matter* **192**, 55 (1993).
- [72] S.-L. Chang, *X-ray Multiple-Wave Diffraction* (Springer-Verlag, Berlin, 2004).
- [73] M. Renninger, *Acta Cryst. A* **24**, 143 (1968).